CrossMark

The 2HWC HAWC Observatory Gamma-Ray Catalog

A. U. Abeysekara[1], A. Albert[2], R. Alfaro[3], C. Alvarez[4], J. D. Álvarez[5], R. Arceo[4], J. C. Arteaga-Velázquez[5], H. A. Ayala Solares[6], A. S. Barber[1], B. Baughman[7], N. Bautista-Elivar[8], J. Becerra Gonzalez[9], A. Becerril[3], E. Belmont-Moreno[3], S. Y. BenZvi[10], D. Berley[7], A. Bernal[11], J. Braun[12], C. Brisbois[6], K. S. Caballero-Mora[4], T. Capistrán[13], A. Carramiñana[13], S. Casanova[14,15], M. Castillo[5], U. Cotti[5], J. Cotzomi[16], S. Coutiño de León[13], E. de la Fuente[17], C. De León[16], R. Diaz Hernandez[13], B. L. Dingus[2], M. A. DuVernois[12], J. C. Díaz-Vélez[17], R. W. Ellsworth[18], K. Engel[7], D. W. Fiorino[7], N. Fraija[11], J. A. García-González[3], F. Garfias[11], M. Gerhardt[6], A. González Muñoz[3], M. M. González[11], J. A. Goodman[7], Z. Hampel-Arias[12], J. P. Harding[2], S. Hernandez[3], A. Hernandez-Almada[3], J. Hinton[15], C. M. Hui[19], P. Hüntemeyer[6], A. Iriarte[11], A. Jardin-Blicq[15], V. Joshi[15], S. Kaufmann[4], D. Kieda[1], A. Lara[20], R. J. Lauer[21], W. H. Lee[11], D. Lennarz[22], H. León Vargas[3], J. T. Linnemann[23], A. L. Longinotti[13], G. Luis Raya[8], R. Luna-García[24], R. López-Coto[15], K. Malone[25], S. S. Marinelli[23], O. Martinez[16], I. Martinez-Castellanos[7], J. Martínez-Castro[24], H. Martínez-Huerta[26], J. A. Matthews[21], P. Miranda-Romagnoli[27], E. Moreno[16], M. Mostafá[25], L. Nellen[28], M. Newbold[1], M. U. Nisa[10], R. Noriega-Papaqui[27], R. Pelayo[24], J. Pretz[25], E. G. Pérez-Pérez[8], Z. Ren[21], C. D. Rho[10], C. Rivière[7], D. Rosa-González[13], M. Rosenberg[25], E. Ruiz-Velasco[3], H. Salazar[16], F. Salesa Greus[14], A. Sandoval[3], M. Schneider[29], H. Schoorlemmer[15], G. Sinnis[2], A. J. Smith[7], R. W. Springer[1], P. Surajbali[15], I. Taboada[22], O. Tibolla[4], K. Tollefson[23], I. Torres[13], T. N. Ukwatta[2], G. Vianello[30], L. Villaseñor[5], T. Weisgarber[12], S. Westerhoff[12], I. G. Wisher[12], J. Wood[12], T. Yapici[23], P. W. Younk[2], A. Zepeda[4,26], and H. Zhou[2]

[1] Department of Physics and Astronomy, University of Utah, Salt Lake City, UT, USA
[2] Physics Division, Los Alamos National Laboratory, Los Alamos, NM, USA
[3] Instituto de Física, Universidad Nacional Autónoma de México, Mexico City, Mexico
[4] Universidad Autónoma de Chiapas, Tuxtla Gutiérrez, Chiapas, Mexico
[5] Universidad Michoacana de San Nicolás de Hidalgo, Morelia, Mexico
[6] Department of Physics, Michigan Technological University, Houghton, MI, USA
[7] Department of Physics, University of Maryland, College Park, MD, USA; riviere@umdgrb.umd.edu
[8] Universidad Politecnica de Pachuca, Pachuca, Hidalgo, Mexico
[9] NASA Goddard Space Flight Center, Greenbelt, MD, USA
[10] Department of Physics & Astronomy, University of Rochester, Rochester, NY, USA
[11] Instituto de Astronomía, Universidad Nacional Autónoma de México, Mexico City, Mexico
[12] Department of Physics, University of Wisconsin-Madison, Madison, WI, USA
[13] Instituto Nacional de Astrofísica, Óptica y Electrónica, Tonantzintla, Puebla, Mexico
[14] Instytut Fizyki Jadrowej im Henryka Niewodniczanskiego Polskiej Akademii Nauk, Krakow, Poland
[15] Max-Planck Institute for Nuclear Physics, Heidelberg, Germany
[16] Facultad de Ciencias Físico Matemáticas, Benemérita Universidad Autónoma de Puebla, Puebla, Mexico
[17] Departamento de Física, Centro Universitario de Ciencias Exactas e Ingenierías, Universidad de Guadalajara, Guadalajara, Mexico
[18] School of Physics, Astronomy, and Computational Sciences, George Mason University, Fairfax, VA, USA
[19] NASA Marshall Space Flight Center, Astrophysics Office, Huntsville, AL, USA
[20] Instituto de Geofísica, Universidad Nacional Autónoma de México, Mexico City, Mexico
[21] Department of Physics and Astronomy, University of New Mexico, Albuquerque, NM, USA
[22] School of Physics and Center for Relativistic Astrophysics, Georgia Institute of Technology, Atlanta, GA, USA
[23] Department of Physics and Astronomy, Michigan State University, East Lansing, MI, USA
[24] Centro de Investigación en Computación, Instituto Politécnico Nacional, Mexico City, Mexico
[25] Department of Physics, Pennsylvania State University, University Park, PA, USA
[26] Physics Department, Centro de Investigación y de Estudios Avanzados del IPN, Mexico City, Mexico
[27] Universidad Autónoma del Estado de Hidalgo, Pachuca, Mexico
[28] Instituto de Ciencias Nucleares, Universidad Nacional Autónoma de México, Mexico City, Mexico
[29] Santa Cruz Institute for Particle Physics, University of California, Santa Cruz, Santa Cruz, CA, USA
[30] Department of Physics, Stanford University, Stanford, CA, USA

Abstract

We present the first catalog of TeV gamma-ray sources realized with data from the newly completed High Altitude Water Cherenkov Observatory (HAWC). It is the most sensitive wide field-of-view TeV telescope currently in operation, with a one-year survey sensitivity of ~5%–10% of the flux of the Crab Nebula. With an instantaneous field of view >1.5 sr and >90% duty cycle, it continuously surveys and monitors the sky for gamma-ray energies between hundreds of GeV and tens of TeV. HAWC is located in Mexico, at a latitude of 19° N, and was completed in 2015 March. Here, we present the 2HWC catalog, which is the result of the first source search performed with the complete HAWC detector. Realized with 507 days of data, it represents the most sensitive TeV survey to date for such a large fraction of the sky. A total of 39 sources were detected, with an expected number of false detections of 0.5 due to background fluctuation. Out of these sources, 19 are new sources that are not associated with previously known TeV sources (association criteria: <0°.5 away). The source list, including the position measurement, spectrum measurement, and uncertainties, is reported, then each source is briefly discussed. Of the 2HWC associated sources, 10 are reported in TeVCat as PWN or SNR: 2 as blazars and the remaining eight as unidentified.

Key words: catalogs – gamma rays: general – surveys

1. Introduction

The High Altitude Water Cherenkov Observatory (HAWC) is a newly completed, very high energy (VHE; >100 GeV) gamma-ray observatory, with a one-year survey sensitivity of ~5%–10% of the flux of the Crab Nebula. The variation in sensitivity depends on the declination of the source under consideration over the observable sky, with declinations between −20° and 60° for the present study. Unlike imaging atmospheric Cherenkov telescopes (IACTs), such as H.E.S.S. (Aharonian et al. 2004), MAGIC (Aleksić et al. 2016), VERITAS (Holder et al. 2006), and FACT (Anderhub et al. 2011), which observe the Cherenkov light emitted by the extensive air showers as they develop in the atmosphere, HAWC detects particles of these air showers that reach ground level, allowing it to operate continuously and observe an instantaneous field of view of >1.5 sr. Prior to this work, unbiased VHE surveys were conducted by the Milagro (Atkins et al. 2003, 2004) and ARGO (Bacci et al. 2002) collaborations. Compared to these previous surface arrays, the sensitivity of HAWC is improved by more than an order of magnitude, thanks to a combination of large detector area, high elevation, and unique background rejection capability. These features make HAWC an ideally suited VHE survey instrument. High-sensitivity surveys of portions of the Galactic plane have also been published by H.E.S.S. (Aharonian et al. 2006b), MAGIC (Albert et al. 2006), and VERITAS (Popkow et al. 2015). At lower energies, the Large Area Telescope on the space-based *Fermi* Observatory (*Fermi*-LAT) has detected many thousands of Galactic and extragalactic gamma-ray sources (Acero et al. 2015), but its small detector area limits its reach into the VHE band.

There are about 200 known VHE gamma-ray sources that have been detected at high significance by a number of observatories (e.g., TeVCat catalog; Wakely & Horan 2008).

Within our Galaxy, these VHE sources include pulsar wind nebulae (PWNe), supernova remnants (SNRs), binary systems, and diffuse emission from the Galactic plane. The SNRs and PWNe represent the majority of the identified sources. Most Galactic sources are observed as spatially extended by IACTs (Carrigan et al. 2013).

Beyond our Galaxy, almost all known TeV sources are Active Galactic Nuclei (AGNs), most of which are categorized as blazars. The TeV gamma-ray emission is generally observed to be variable, and thought to originate from one or more regions of particle acceleration in the jet. Although gamma-ray emission has been observed up to energies of about 10 TeV for some blazars (Aharonian et al. 2001; Acciari et al. 2011), the flux at and beyond such energies is strongly attenuated as a function of distance, due to photon–photon interaction with the extragalactic background light (EBL). Because the sensitivity of HAWC peaks around 10 TeV (depending on the source spectrum and declination, see Section 4.4 for details), where absorption of TeV photons through the infrared component of the EBL becomes severe, the sensitivity of the HAWC survey to distant AGNs is relatively poor.

Many VHE sources are not identified (a fifth of TeVCat sources are reported as unidentified). The principal gamma-ray production mechanisms are the leptonic and hadronic processes, where VHE photons originate from an initial population of accelerated particles (leptons and hadrons) via inverse Compton scattering and π^0-decay, respectively. The gamma-ray spectrum alone is generally not sufficient to uniquely identify the emission process. In both cases, the gamma-ray emission is accompanied by a lower-energy synchrotron emission, whether from the original lepton population in the leptonic case, or from secondary leptons in the hadronic case. Other possible gamma-ray production mechanisms include, for instance, the decay or annihilation of dark matter particles, although no definitive detection has been reported so far. Multi-wavelength and morphological studies are essential to identify the sources of very high-energy gamma rays and their emission mechanisms. The present catalog represents an initial contribution to this effort by using HAWC to detect new sources and characterize both new and previously known sources using the ground-detection technique.

Compared to IACTs, HAWC's angular resolution is larger and its peak sensitivity is shifted to higher energies (Abeysekara et al. 2017b). Consequently, comparison of source significance and flux with IACT observations requires careful examination: the HAWC instrument is relatively more sensitive to sources with harder energy spectra than softer ones, and HAWC loses relatively less sensitivity than IACTs when the source gets larger. On the other hand, the surface detection method employed by HAWC permits continuous day and night observation of the entire overhead sky, under all weather conditions. For sources that transit through its field of view, HAWC typically accumulates 1500–2000 hr yr^{-1} of total exposure. Thus, above 10 TeV, where photon statistics are poor, HAWC achieves better sensitivity than even long-duration observations by IACTs (see, e.g., last figure of Abeysekara et al. 2017b, where the quarter-decade point source sensitivity to the Crab PWN surpasses a 50 hr observation by current-generation IACTs above 10 TeV).

This paper presents a catalog of TeV gamma-ray sources resulting from a search for significantly enhanced point and extended emission, detected in the gamma-ray sky maps of 17 months of HAWC data. More detailed morphology studies will be the subject of future papers.

In Section 2, we describe the HAWC detector. Section 3 describes the analysis of gamma-ray events, and construction of our source catalog. Results and discussion are provided in Sections 4–6. Conclusions and an outlook are in Section 7.

2. HAWC Detector

The HAWC detector is located in central Mexico at 18°59′41″N 97°18′30″.6W and an elevation of 4100 m a.s.l. The instrument comprises 300 identical water Cherenkov detectors (WCDs) made from 5 m high, 7.32 m diameter, commercial water storage tanks. Each tank contains a custom-made, light-tight bladder to accommodate 190,000 l of purified water. Four upward-facing photomultiplier tubes (PMTs) are mounted at the bottom of each tank: a 10″ Hamamatsu R7081-HQE PMT positioned at the center, and three 8″ Hamamatsu R5912 PMTs positioned halfway between the tank center and rim. The central PMT has roughly twice the sensitivity of the outer PMTs, due to its superior quantum efficiency and larger size. The WCDs are filled to a depth of 4.5 m, with 4.0 m (more than 10 radiation lengths) of water above the PMTs. This large depth guarantees that the electrons, positrons, and gammas in the air shower are fully absorbed by the HAWC detector, well above the PMT level, so that the detector itself acts as an electromagnetic (EM) calorimeter providing an accurate measurement of EM energy deposition. High-energy
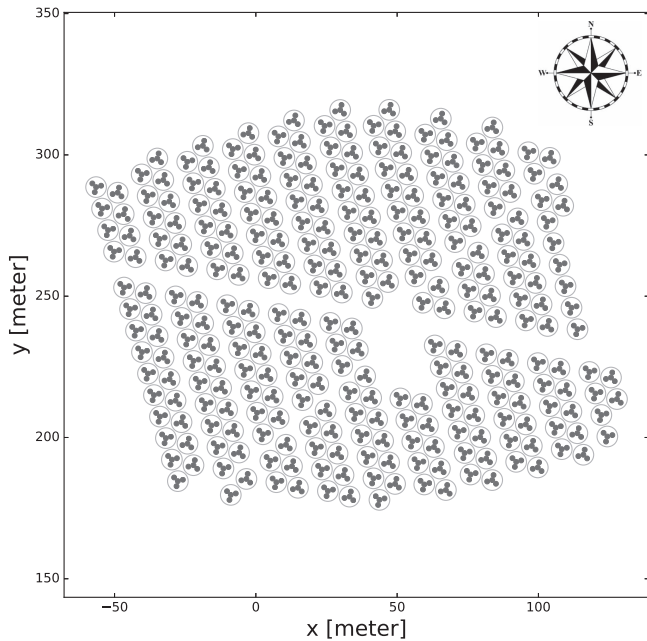
Figure 1. Layout of HAWC WCDs and positions of the PMTs (PMTs not to scale). The conspicuous gap indicates the location of the counting house, which is centrally located to minimize the cable length.

electrons are detected via the Cherenkov light they produce in the water, and gamma rays are converted to electrons through pair production and Compton scattering. Muons are also detected. They are more likely to be produced in air showers originating from hadronic cosmic-ray interactions with the atmosphere, and tend to have higher transverse momentum, producing large signals in the PMTs far from the air shower axis. Thus, they serve as useful tags for rejecting hadronic backgrounds. The WCDs are arranged in a compact layout to maximize the density of the sensitive area, with about 60% of the $22,000 \, m^2$ detector area instrumented. See Figure 1 for a diagram of the HAWC detector.

Analog signals from the PMTs are transmitted by RG-59 coaxial cable to a central counting house. The signals are shaped and discriminated at two voltage thresholds, roughly corresponding to 1/4 photoelectron (PE) and 4 PEs. The threshold crossing times (both rising and falling) are recorded using CAEN V1190A time-to-digital converters (Abeysekara et al. 2017b). Individual signals that pass at least the low threshold are called hits. The time-over-threshold is used to estimate the charge. The response of this system is roughly logarithmic, such that the readout has reasonable charge resolution over a very wide dynamic range, from a fraction of 1 PE to 10,000 PEs. The timing resolution for large pulses is better than 1 ns. All channels are read out in real time, with zero dead time, and blocks of data are aggregated in a real-time computing farm. A trigger is generated when a sufficient number of PMTs record a hit within a 150 ns window (28 hits were required for most of the data used in this analysis, although other values were occasionally used earlier). This results in a ~20 kHz trigger rate. Small events, with a number of hits close to the threshold value, which dominate the triggers, require a specific treatment; they are removed from the analysis presented here. In the future, their inclusion will significantly lower the energy threshold of HAWC. For sources with spectra that extend beyond 1 TeV, like the Crab Nebula, the sensitivity usually peaks above 5 TeV (depending on the

source spectrum and declination). Excluding near-threshold events does not significantly reduce the sensitivity. Details of our event selection for this analysis are presented in the next section.

For each triggered event, the parameters of the air shower, like the direction, size, and some gamma/hadron separation variables, are extracted from the recorded hit times and amplitudes with the help of a shower model developed through the study of Monte Carlo simulations and optimized using observations of the Crab Nebula (Abeysekara et al. 2017b). The angular resolution of the HAWC instrument varies with the event size (number of hit PMTs). It ranges from $\sim0°.2$ (68% containment) for large events events hitting almost all the PMTs, to $\sim1°.0$ for events near the analysis threshold.

Gamma-ray induced showers are generally compact, with a smooth lateral distribution around the shower core (where the shower axis intersects the detector plane). In contrast, hadronic background events tend to be broader, contain multiple or poorly defined cores, and include highly localized, large signals from muons and hadrons at significant distance from the shower axis. Selection cuts on shower morphology eliminate >99% of the hadronic background in the large event-size samples, and at least 85% of the background near the analysis threshold, while usually retaining more than 50% of the gamma-ray induced signal events. Details of the data reconstruction, analysis, and verification of the sensitivity of the measurement will be presented in a future publication on the observation of the Crab Nebula with the HAWC Observatory (Abeysekara et al. 2017b).

3. Methodology

In this section, we review the details of the data set used in the analysis, and describe the event selection and construction of unbiased maps of the viewable sky, which include estimates of the cosmic-ray background rates. From the maps, we compute a test statistic (TS) based on the ratio of the likelihood that a source is present and the null hypotheses that the observed event population is due to background alone. We identify and localize sources from a list of local maxima in the TS maps with values greater than 25. The procedure is applied to the map to identify point-like sources, as well as sources with characteristic sizes $0°.25$, $0°.5$, $1°$, and $2°$. Many sources, particularly the bright ones, will likely be detected in both the point-source and extended-source maps. We find that there are some extended regions of gamma-ray emission that could be interpreted as either a single extended source or an ensemble of point sources. Below, we describe the method employed to detect point and extended sources, to estimate their positions, extents, and spectra, and finally discuss the principal sources of systematic uncertainty.

3.1. Data Set

The results presented here are from data taken between 2014 November 26 and 2016 June 02. During this period, 8.8×10^{11} triggered events were recorded to disk. The full HAWC Observatory was inaugurated on 2015 March. During the construction phase, prior to the inauguration, data were collected with a variable number of WCDs, ranging from 250 to 300. Overall, there were 40 days of downtime (7.2%) during this 553 day period, mostly related to power issues or

Table 1
Properties of the Nine Analysis Bins: Bin Number $\mathcal{B}$, Event Size f_{hit}, 68% PSF Containment ψ_{68}, Cut Selection Efficiency for Gammas $\epsilon_\gamma^{\text{MC}}$ and Cosmic Rays $\epsilon_{\text{CR}}^{\text{data}}$, and Median Energy for a Reference Source of Spectral Index -2.63, at a Declination of $20°$ $\tilde{E}_\gamma^{\text{MC}}$

$\mathcal{B}$	f_{hit} (%)	ψ_{68} (°)	$\epsilon_\gamma^{\text{MC}}$ (%)	$\epsilon_{\text{CR}}^{\text{data}}$ (%)	$\tilde{E}_\gamma^{\text{MC}}$ (TeV)
1	6.7–10.5	1.03	70	15	0.7
2	10.5–16.2	0.69	75	10	1.1
3	16.2–24.7	0.50	74	5.3	1.8
4	24.7–35.6	0.39	51	1.3	3.5
5	35.6–48.5	0.30	50	0.55	5.6
6	48.5–61.8	0.28	35	0.21	12
7	61.8–74.0	0.22	63	0.24	15
8	74.0–84.0	0.20	63	0.13	21
9	84.0–100.0	0.17	70	0.20	51

scheduled shutdowns for construction or maintenance. In addition, seven days of data (1.3%) were removed based on requirements regarding the stability of the detector performance. The final livetime used for the analysis is 506.6 days, corresponding to a 92% duty cycle.

The data were reconstructed and analyzed with *Pass 4*, which includes improved calibrations and event reconstruction, as well as improvements in the likelihood framework used for the map analysis. The new event reconstruction benefits from a directional fit using an improved shower model, a new algorithm to separate gamma-ray and hadronic events, and a better electronics model. For comparison, our previous search for sources in the inner Galactic plane, which defined the 1HWC source list (Abeysekara et al. 2016), was performed using 275 days of data taken with a detector consisting of about one third of the full HAWC array, using the *Pass 1* analysis. This new pass, combined with the larger detector and longer exposure time, improves the sensitivity of the survey by about a factor of five, with respect to the *Pass 1* inner Galactic Plane search.

3.2. Event Selection

Events are classified by size in nine analysis bins $\mathcal{B}$, presented in Table 1, depending on the fraction f_{hit} of active PMTs in the detector that participate in the reconstruction of the air shower. We chose to define bins based on the fraction of the detector hit, rather than the absolute number of PMTs, in order to obtain more stable results for the various detector configurations of active WCDs over time.

The selection cuts on the gamma/hadron separation variables are optimized for each bin, using observations of the Crab Nebula (Abeysekara et al. 2017b). The point-spread function (PSF) of the reconstructed events depends on the event size. In Table 1, the ψ_{68} column represents the 68% containment angle of the PSF, for a source similar to the Crab Nebula. Large events have better PSF and hadronic background rejection, and correspond to higher-energy primary particles. The efficiency of the gamma/hadron separation cuts is indicated in the $\epsilon_\gamma^{\text{MC}}$ and $\epsilon_{\text{CR}}^{\text{data}}$ columns, where the gamma efficiency has been estimated using Monte Carlo simulation of the detector, and the hadron efficiency has been measured directly using cosmic-ray data. The $\tilde{E}_\gamma^{\text{MC}}$ column represents the median energy of the simulated gamma-ray photons in this analysis bin, for a source at a declination of $20°$ and an energy

spectrum $E^{-2.63}$ (Crab Nebula-like source). Events in the same bin for a source with a harder spectrum, or at larger declination, will tend to have larger energy on average.

3.3. Event and Background Maps

After reconstruction, event and background maps are generated. The event maps are simply histograms of the arrival direction of the reconstructed events, in the equatorial coordinate system. The background maps are computed using a method developed for the Milagro experiment, known as direct integration (Atkins et al. 2003). It is used to fit the isotropic distribution of events that pass the gamma-ray event selection, while accounting for the asymmetric detector angular response and varying all-sky rate. As strong gamma-ray sources would bias the background estimate, some regions are excluded from the computation. These regions cover the Crab, two Markarians, and the Geminga region, as well as a region $\pm3°$ around the inner Galactic Plane. Nine event maps and nine background maps are generated, for the nine analysis bins.

The maps are produced using a HEALPix pixelization scheme (Górski et al. 2005), where the sphere is divided in 12 equal-area base pixels, each of which is subdivided into a grid of $N_{\text{side}} \times N_{\text{side}}$. For the present analysis, maps were initially done using $N_{\text{side}} = 1024$ for a mean spacing between pixel centers of less than $0°.06$, which is small compared to the typical PSF of the reconstructed events (as shown on Table 1).

3.4. Catalog Construction

The maximum likelihood analysis framework presented in Younk et al. (2016) is used to analyze the maps. The TS is defined using the likelihood ratio

$$\text{TS} = 2 \ln \frac{\mathcal{L}^{\text{max}}(\text{Source Model})}{\mathcal{L}(\text{Null Model})}, \qquad (1)$$

to compare a source model hypothesis with a null hypothesis. The likelihood of a model $\mathcal{L}(\text{Model})$ is obtained by comparing the observed event counts to the expected counts, for all the pixels in a region of interest, and all nine analysis bins, as detailed in Section 4.1. of Abeysekara et al. (2017b). Here, we test the presence of a single source at a time, without adding other potential nearby sources to the model, i.e., the source model consists of the background (as in the null hypothesis) plus a single test source.

In order to take advantage of HAWC's sensitivity to both point-like and extended sources, four searches are conducted to test for either point or extended sources ($0°.5$, $1°$, and $2°$ radius). The TS maps used for the search are computed using a test source with a fixed geometry (point source or uniform disk of fixed radius) and an energy spectrum consisting of a power law of fixed index,

$$dN/dE = F_0(E/E_0)^\alpha, \qquad (2)$$

where E_0 is a reference energy, F_0 is the differential flux at E_0, and α is the spectral index.

For the null model, the values from the direct integration background maps are used as the expected counts. For the source model, the expected counts number comprises an additional signal contribution from the source, derived using the source characteristics and detector response from
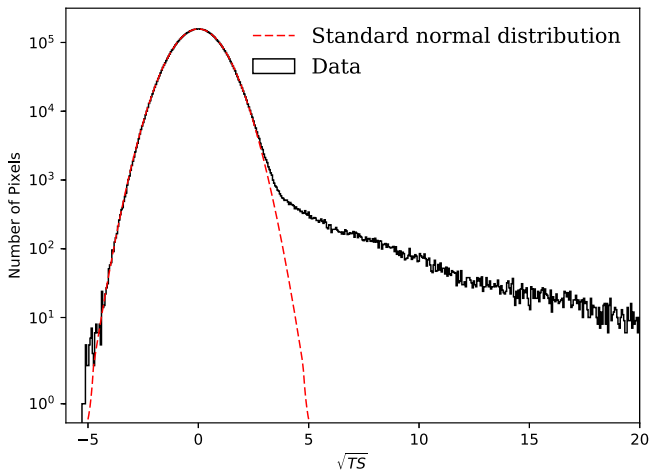
Figure 2. Test statistic distribution of the point source search (black) and standard normal distribution (red).

simulation (expected counts for the spectrum and PSF, both functions of the analysis bin, and the declination).

The TS is maximized with respect to the free parameters of the source model. This approach is first used to search for sources, with F_0 as the only free parameter. Once the source locations are defined, the likelihood framework is used again to measure the energy spectrum of said sources as a result of the TS maximization (where both F_0 and α are free during the maximization); cf., Section 3.6.

For the source searches, TS maps are made by moving the location of the hypothetical source across the possible locations in the sky. The source and null models are nested; hence, by Wilks' Theorem, the TS is distributed as χ^2 with one degree of freedom, if the statistics are sufficiently large. Consequently, the pre-trial significance, conventionally reported as standard deviations (sigmas), is obtained by taking the square root of the TS, $\sqrt{TS}$ (here and after, what we denote $\sqrt{TS}$ actually corresponds to $\mathrm{sign}(TS)\sqrt{|TS|}$). Figure 2 shows the distribution of $\sqrt{TS}$ across the sky for the point source search, as well as a standard normal distribution scaled by the number of pixels. For values lower than ~ 3, the $\sqrt{TS}$ is reproduced well by the normal distribution, whereas a large excess can be seen, due to the presence of sources in the sky, at greater values.

Prior to the catalog search, the energy spectrum of the known TeVCat sources that can be considered point-like given the angular resolution of the HAWC instrument, specifically those with dimensions (reported by TeVCat) to be $<0\overset{\circ}{.}1$, were fit using HAWC data. The resulting spectral indices ranged from approximately -3.1 to -2.5, usually around -2.7, which is typically softer than the indices listed in TeVCat. This can be explained if the sources soften or cut off at the energies observed by HAWC. Consequently, a spectral index of -2.7 is used for the point source search for self-consistency. On the other hand, the Geminga PWN, which was first observed at TeV energies by the Milagro collaboration (Abdo et al. 2009), is detected by HAWC with an extent of about $2°$ and a hard spectral index around -2. To account for the range of source extents and spectra observed with HAWC, four different maps were used to build the catalog, testing various source hypotheses. In order to limit computing time, the resolutions of the maps are adapted to the characteristic dimension of the hypothetical source, without significantly affecting the results:

1. A point source map of index -2.7 (HEALPix map resolution $N_{\mathrm{side}} = 1024$ or $0\overset{\circ}{.}06$ per pixel).
2. An extended source map of radius $0\overset{\circ}{.}5$ and index -2.0 ($N_{\mathrm{side}} = 512$ or $0\overset{\circ}{.}1$ per pixel).
3. An extended source map of radius $1\overset{\circ}{.}0$ and index -2.0 ($N_{\mathrm{side}} = 256$ or $0\overset{\circ}{.}2$ per pixel).
4. An extended source map of radius $2\overset{\circ}{.}0$ and index -2.0 ($N_{\mathrm{side}} = 256$ or $0\overset{\circ}{.}2$ per pixel).

Extended searches tend to merge nearby sources that could be resolved in point source or less extended searches. To limit this effect, the catalog is initially generated based on the point source search, then the sources from the extended searches, ordered by increasing radius, are added. However, a strong extended source may be found in the point source search, possibly multiple times (see, e.g., Geminga below), as well as in the extended search. Hence, the exact search in which a source is first tagged should not be regarded as a measurement of the source extent. However, an isolated source first found in an extended search may be a hint of extension. More robust morphology studies will be performed in a future analysis, but are beyond the scope of this catalog paper.

To select the sources in the maps, all local maxima with TS > 25 are flagged. In some regions, multiple local maxima are found very near each other. We define primary sources as all local maxima that are separated from neighboring local maxima of higher significance by a valley of $\Delta(\sqrt{TS}) > 2$. We also define and include secondary sources when $1 < \Delta(\sqrt{TS}) < 2$. These sources are marked with an asterisk (*).

The final catalog comprises the sources of the point source search plus the sources of the extended searches, ordered by increasing radius, if their locations are more than $2°$ away from any hotspot with TS greater than 25 in the previous searches.

3.5. False Positive Expectation

When selecting the sources in the map, a background fluctuation can sometimes mimic a source and fulfill the selection criteria. To estimate this possible contamination, the search was run on randomized background maps. Events maps are generated for each of the nine analysis bins, and then the full search strategy (as for the data map) is employed, including point and extended source searches, as detailed on Section 2. This complete procedure was run with 20 sets of simulated maps. In 11 cases, no sources were flagged. In nine cases, one source was flagged. In total, out of the 20 full searches performed over the entire sky, nine sources were flagged, so the predicted number of background fluctuations passing the TS > 25 criterion is about $9/20 = 0.45$. Therefore, the predicted number of false positive in the catalog is about 0.5. These possible fluctuations are typically close to the threshold value TS = 25, and are usually out of the Galactic Plane, as it only represents a small fraction of the visible sky.

3.6. Source Position, Extent, and Energy Spectrum

The source positions reported in this catalog correspond to the first search in which they appear, as presented in Section 2. The statistical uncertainty of the position is defined as the maximum distance between the center and the one-sigma contour obtained from the TS map.

After the search, a residual map is generated and halo-like structures are visible around several sources modeled as point

sources, possibly indicating that these sources could be extended. Although no automatic procedure was used to characterize these extents,[31] tentative source radii were manually defined while looking at these residual maps. These radii were used as a secondary source model when fitting the energy spectrum (results presented in Table 3 of the next section). These should not be regarded as measurements of the source extents, but can nonetheless provide useful information on how much the spectrum measurement depends on the source region definition. When this new source region definition is a good representation of the actual source, the newly fitted spectrum should better correspond to the source spectrum. However, as it corresponds to a larger region, it is more subject to contamination from other sources or possibly diffuse emission. Additionally, for some complex regions, or regions for which independent analyses are performed, the whole region is fit, explicitly including multiple sources, as an estimate of the total flux of the region. Such regions are discussed in Section 5.

Once the source location and size are defined, the source spectrum is fit using the maximum likelihood method presented in Section 2, where the source geometry is fixed (point source or extended source of fixed radius) and the energy spectrum is free (the power law of Equation (2), where F_0 and α are free). For the range of declinations considered, the reference energy of 7 TeV minimizes the correlation between the index and normalization, as this reference energy corresponds to the region of maximum sensitivity (cf., right side of Figure 10). We report the differential flux at 7 TeV (F_7), the index α, and the statistical uncertainties on both parameters in Table 3.

3.7. Systematic Uncertainties

The absolute pointing of the HAWC Observatory is initially determined using a careful survey of the WCDs and PMTs, and then refined using the observed position of the Crab Nebula. The positions of Markarian 421 and Markarian 501 are observed by HAWC within $0°.05$ of their known locations after the pointing calibration. Additional studies based on the observation of the Crab Nebula when it is farther from zenith showed that absolute pointing is still better than $0°.1$, up to a zenith angle of $45°$, which covers the full declination range considered in the present study. Therefore, the systematic uncertainty on the absolute pointing of the catalog is quoted as $0°.1$.

For isolated point sources, the systematic uncertainties on the spectrum measurement are estimated to be $\pm 50\%$ for the overall flux and ± 0.2 for the spectral index (Abeysekara et al. 2017b). In the present analysis, no detailed morphology study is performed. However, there is a correlation between the assumed source size and the measured spectrum. Simulation studies show that, for isolated sources, the unknown extent can induce an additional systematic uncertainty on the spectral index measurement of up to 0.3. This can also be seen in the results for the sources measured under different size assumptions in Table 3). Similarly, the reported flux normalization F_7 can be significantly affected by the assumed source size, up to a factor of a few for very extended sources or confused regions. The fluxes of sources that appear extended are reported in Table 3, with multiple extent hypotheses, to bracket this effect.

As we test the presence of a single source at a time without modeling the other sources, the likelihood computation may be impacted by events from a neighboring source. This is particularly true for lower-energy events where the PSF is wider. By adding events to the single hypothesized source, this contamination can increase the measured flux and make the spectral index softer. In the case of two identical point sources located $1°$ apart, the flux measurement, assuming a known spectral index, is increased by 20%–30%, depending on the declination. When fitting the index as well, the index can change by up to 0.1, and the measured flux is changed by about 20%–40%. This confusion is considered a systematic uncertainty of the present analysis, and tends to be larger in very populated regions of the sky with high source populations.

4. Results

We present the result of our search—the 2HWC catalog. A total of 39 sources are found,[32] four of which are detected only with the extended search procedure. As discussed in Section 3.5, the predicted number of background fluctuations passing the selection criteria is about 0.5.

4.1. Maps

The TS map derived from the all-sky search for point sources with index -2.7 is presented in equatorial coordinates in Figure 3. The inner Galactic plane is clearly visible. In the outer Galactic plane, the Crab and Geminga are visible. Outside the Galactic plane, Markarian 421 and Markarian 501 stand out.

Figures 4–8 show detailed views of smaller regions of the sky; 2HWC sources are represented by white crosses and labels below them. The source locations listed in TeVCat are also marked with black circles and labels above those symbols.

The maps of the regions around the Crab, Markarian 421, and Markarian 501 are shown in Figure 4. The region of the outer Galactic Plane around Geminga is mapped in Figure 5. The left map shows the result of the point source search; the right map that of the $2°$ extended search. The increased TS in the extended search supports the case of a significant extent of the two TeV sources detected by the HAWC Observatory in this region. Isolated sources found out of the Galactic plane are shown in Figure 6. Finally, the inner Galactic plane, from the Cygnus region toward the center of the Galaxy, is shown in Figures 7 and 8.

4.2. Catalog

Table 2 lists all sources found using the procedure described in Section 2, ordered by right ascension. The first column lists the HAWC catalog name. The second column specifies the search in which the source first appeared with a TS above the threshold value of 25. PS denotes the point source search, with $0°.5$, $1°$, and $2°$ as the disk radius of the extended search. The corresponding TS value is reported in the third column. The following columns compile the source positions in equatorial (J2000.0 epoch) and Galactic coordinates, as well as the one-sigma uncertainty of the position of the maximum identified in the respective search. The second part of the table, after the vertical line, provides information on the nearest TeVCat

---

[31] Such a procedure was tested and works reasonably well for isolated sources, but most of the sources of the catalog are not isolated.

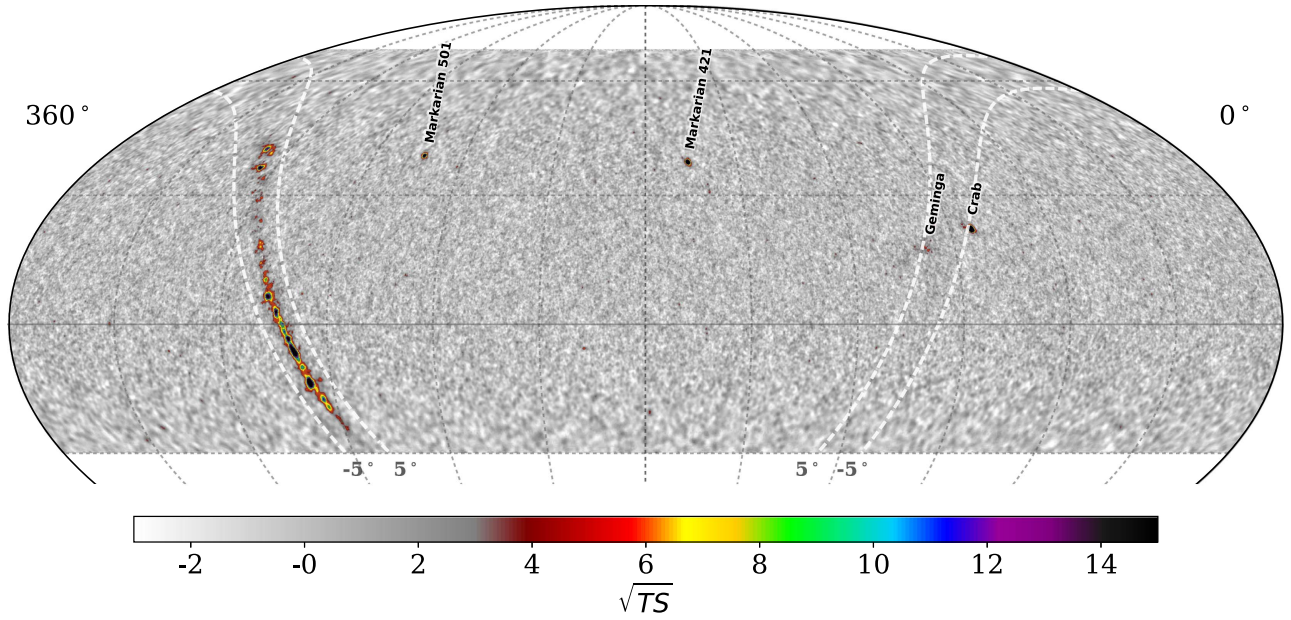[32] Geminga is flagged twice, but only counted as one here.

Figure 3. Equatorial full-sky TS map, for a point source hypothesis with a spectral index of -2.7. Black graticule corresponds to the equatorial coordinate system, and white lines indicate Galactic latitudes $\pm5°$.
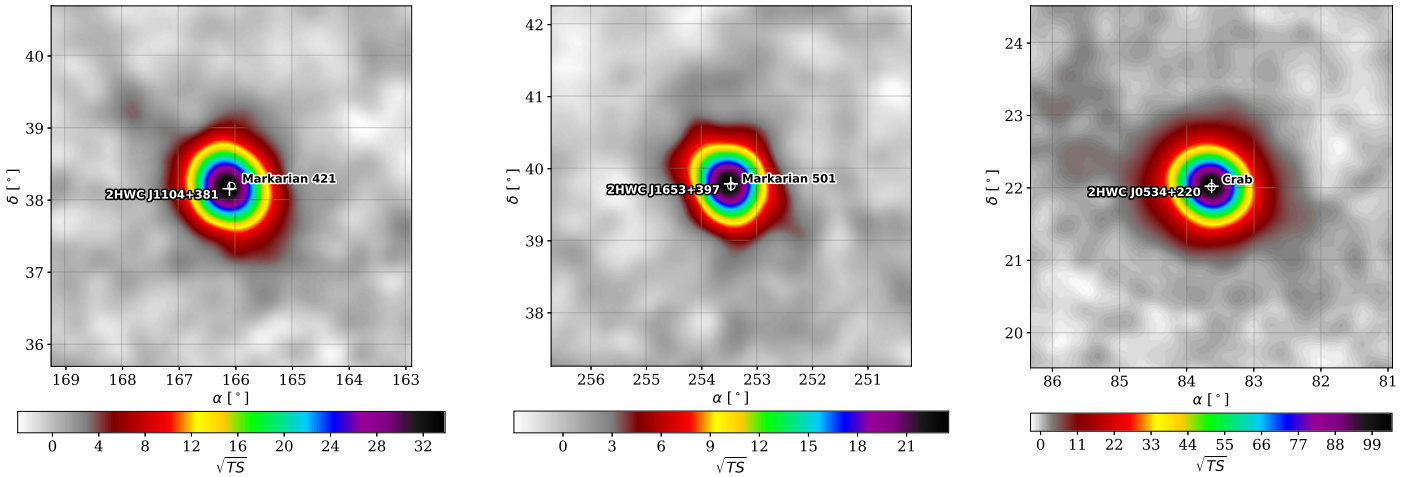

Figure 4. Regions around Markarian 421, Markarian 501, and the Crab Nebula: equatorial TS maps, for a point source hypothesis with a spectral index of -2.7. In this figure and the following, 2HWC sources are represented by white crosses and labels below them, whereas the sources listed in TeVCat are represented with black circles and labels above them.

source: the distance, then the corresponding name if this distance is less than $0°\!.5$. This reference to the nearest TeVCat source is only indicative and not a claim of identification. Each source is briefly discussed in Section 5.

Table 3 lists the differential photon flux at 7 TeV (F_7) and the spectral index of the power law that fit the source identified in HAWC data best. For all sources, we report the flux estimated with the source model corresponding to the search in which the source was found. For the sources for which an additional source size hypothesis was defined, as detailed in Section 3.6, the second flux measurement is also reported.

The results of Table 3 are illustrated in Figure 9. For fluxes $F_7 > 3 \times 10^{-14}\,\mathrm{TeV^{-1}\,cm^{-2}\,s^{-1}}$, all sources have previously been detected using other instruments, but the fraction of newly detected sources dominates the sample below this value. We note here that, when taking into account the full extent of each source, the Crab Nebula is only the third-brightest source in the

sky at 7 TeV. The brightest sources are 2HWC J1837$-$065 and 2HWC J1825$-$134.

In Figure 9, there is a region around $F_7 = 0.8 \times 10^{-15}\,\mathrm{TeV^{-1}\,cm^{-2}\,s^{-1}}$ and power-law index <-2.7, where new catalog sources cluster. These sources do not have significant flux beyond the PSF of HAWC, and therefore should provide interesting targets for follow-up with IACTs.

4.3. Diffuse Galactic Emission

At GeV energies, diffuse emission resulting from the interaction of cosmic rays with matter and photons is the dominant component of the gamma-ray sky. This diffuse emission has a steeper spectrum than Galactic gamma-ray sources, and the TeV sky is source-dominated as a result. The Milagro and H.E.S.S. experiments measured the TeV diffuse emission in Abdo et al. (2008) and Abramowski et al. (2014).
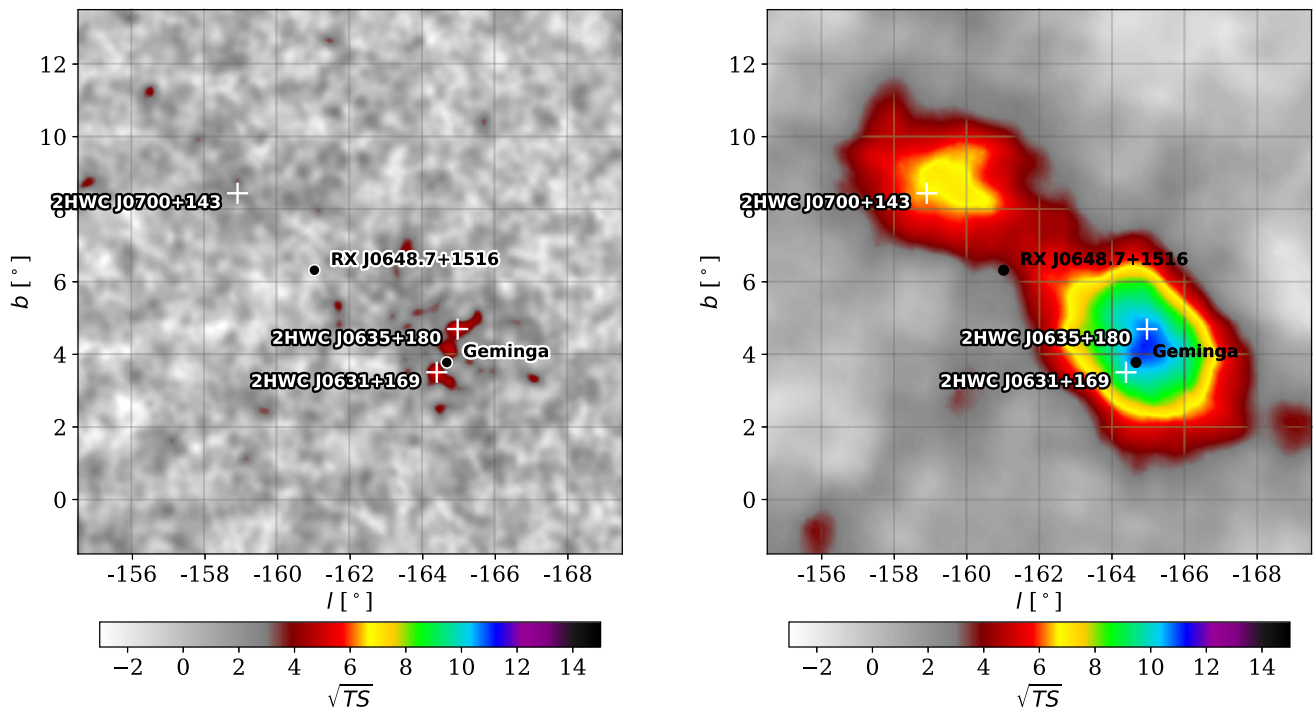
Figure 5. Region around Geminga, in Galactic coordinates. Left: TS map for a point source hypothesis with a spectral index of -2.7. Right: TS map for an extended source hypothesis represented by a disk of radius of $2°\!.0$, with a spectral index of -2.0. Here, 2HWC J0700+143 is not visible in the point source search, but is detected in the extended search.

Both measured a higher flux than predicted—by the numerical cosmic-ray propagation code GALPROP (Strong et al. 2007) for Milagro,[33] and a hadronic model for H.E.S.S., likely due to unresolved sources. A diffuse emission is not included in the likelihood model used in the present analysis. We are concerned that sources identified by this analysis may have a significant underlying diffuse component, or in extreme cases, arise from background fluctuations in a continuous region of diffuse emission. To estimate the maximum possible contribution of the diffuse emission to the spectrum measurement, we ran the search on randomized maps. An additional isotropic flux per steradian was added atop these maps, with a normalization corresponding to the peak flux value of the hadronic model reported by H.E.S.S.(1×10^{-9} TeV^{-1} cm^{-2} s^{-1} sr^{-1} at 1 TeV) and a spectral index of -2.7. We estimate that, for the low-latitude sources near the detection threshold (where the diffuse contribution will be the largest), the diffuse emission can contribute to $<30\%$ of the fluxes measured with the point source hypothesis. The contribution may be larger in extended sources, possibly up to 100% in the worst-case scenario; a $2°$ source with a soft spectrum, at declination $20°$. However, 2HWC J1949+244 is the only source in the plane that was found in the extended search, and the contribution of the diffuse to the fitted flux estimated by this method is $<40\%$.

As an alternative method of estimating the contribution from Galactic diffuse emission, we can use a region of the Galactic plane with no detected sources to derive a conservative upper limit on this contribution. As with the analyses by HESS and Milagro mentioned above, this approach will naturally overestimate the diffuse component because it includes unresolved sources. We

use the region with longitude l between $56°$ and $64°$ and latitude $|b| < 0°\!.5$, which does not contain detected sources. The median differential flux at 7 TeV measured in this region with the point source model is 2.1×10^{-15} TeV^{-1} cm^{-2} s^{-1}. This small excess over a large region indicates the presence of either the Galactic diffuse emission, some unresolved sources, or more likely a combination of both. We use it as a conservative estimate of the impact of the diffuse on the flux of the sources measured in the plane near $l = 60°$. We extrapolate to lower latitudes using the shape of the longitudinal profile of the diffuse emission from GALPROP in Abdo et al. (2008). Using this approach, we find that the diffuse emission can contribute up to 60% of the flux measurement of the weak, low-latitude sources (TS close to 25) that have longitudes between $34°$ and $50°$. For $l > 50°$, the modeled diffuse emission is lower; for $l < 34°$, all the detected sources have higher fluxes that are not impacted significantly by the diffuse emission. The sources for which this conservative estimate is above 30% of the measured point source flux at 7 TeV are: 2HWC J1852+013*, 2HWC J1902+048*, 2HWC J1907 +084*, 2HWC J1914+117*, 2HWC J1921+131, and 2HWC J1922+140, as defined and discussed in Sections 4 and 5. In the likely case where part or most of the flux measured in the $l = [56°, 64°]$ region indeed contains unresolved sources, the diffuse flux is lesser, and so is its contribution to the flux reported on this catalog.

Future dedicated analysis of the HAWC data will allow us to better constrain the Galactic diffuse emission.

4.4. HAWC Performance

Due to the development of air showers in the atmosphere, HAWC's sensitivity and energy response vary with the source declination. The sensitivity of the point source search is represented in Figure 10, left. The curves correspond to the flux

---

[33] The conventional GALPROP version is used here, because the optimized version was derived to fit the EGRET excess, which was latter refuted by *Fermi*-LAT.
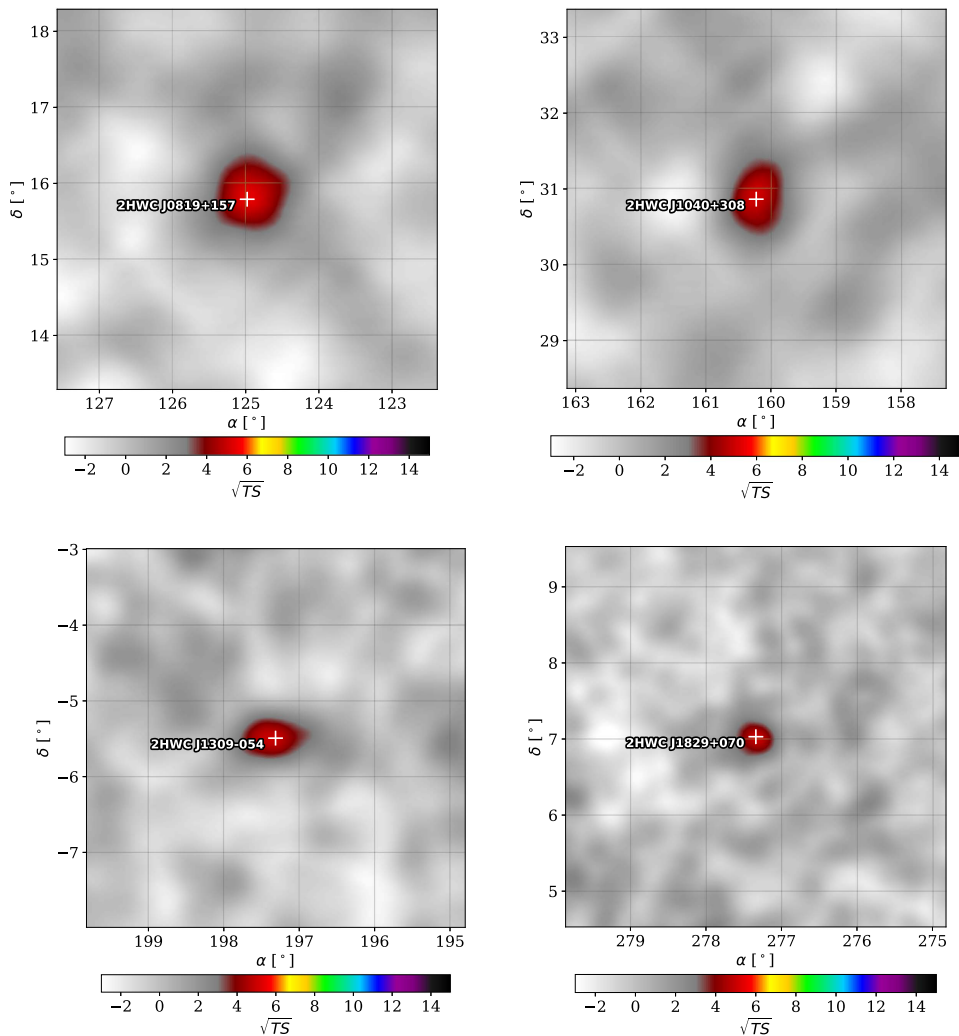
Figure 6. Regions around 2HWC J0819+157, 2HWC J1040+308, 2HWC J1309−054, and 2HWC J1829+070 in equatorial coordinates. The TS maps correspond to the search in which these sources were found: the extended source hypothesis with a radius of 0°.5 and a spectral index of −2.0 for the former two, and the point source hypothesis and spectral index of −2.7 for the latter two.

that gives a central expectation of a 5σ signal for point sources with power-law fluxes of indices −2.0, −2.5, and −3.0, respectively. The maximum sensitivity is obtained for sources transiting at the zenith of HAWC, i.e., whose declinations are close to 19°. The sources found in the point source search are also represented here: the measured flux and statistical uncertainty are shown at the corresponding declination.

The energy range that contributes to most of the TS in the point source search, derived from simulation, is represented in Figure 10, right. More precisely, assuming a given spectral model, we show the energy range as the energy defining the central 50% of the contribution to the TS. Three spectral models are represented: power laws of index −2.0, −2.5, and −3.0, respectively. For a given spectral model, the energy range that contributes most of the TS shifts to lower values for sources transiting overhead than for those whose declinations are far from 19°.

5. Discussion

In this section, we briefly discuss each source, ordered by right ascension. We review their association with previously known TeV sources and possible counterparts at other wavelengths. Hereafter, we define "association" with a HAWC source as a simple spatial coincidence within 0°.5 of the 2HWC

position. Of particular interest are the sources detected with previous and current TeV instruments, including the 1HWC sources observed in the inner Galaxy with a partial configuration of HAWC (Abeysekara et al. 2016) and sources listed in TeVCat. GeV counterparts are also searched in the *Fermi*-LAT catalogs: the standard 2FGL and 3FGL catalogs (Abdo et al. 2010a; Nolan et al. 2012; Acero et al. 2015), the high energy 1FHL and 2FHL catalogs (Ackermann et al. 2013, 2016), the second pulsar catalogs (Abdo et al. 2013), and the SNR catalog (Acero et al. 2016). The ATNF pulsar catalog (Manchester et al. 2005) is used to look for nearby pulsars. When available, the pulsars spindown power $\dot{E}$, distance d, and age τ are reported, as obtained from the ATNF catalog unless mentioned otherwise.

5.1. 2HWC J0534+220—Crab

2HWC J0534+220 is the source with the largest significance in this catalog, with TS = 1.1×10^4. It corresponds to the Crab PWN, which was the first TeV source detected, in 1989 (Weekes et al. 1989), and which has since been commonly used as a calibration source for TeV instruments. The corresponding pulsar is young and has a high spindown power ($\dot{E} = 4.5 \times 10^{38}$ erg s^{-1}, $d = 2.0$ kpc, $\tau = 1.26$ kyr). In the GeV regime,
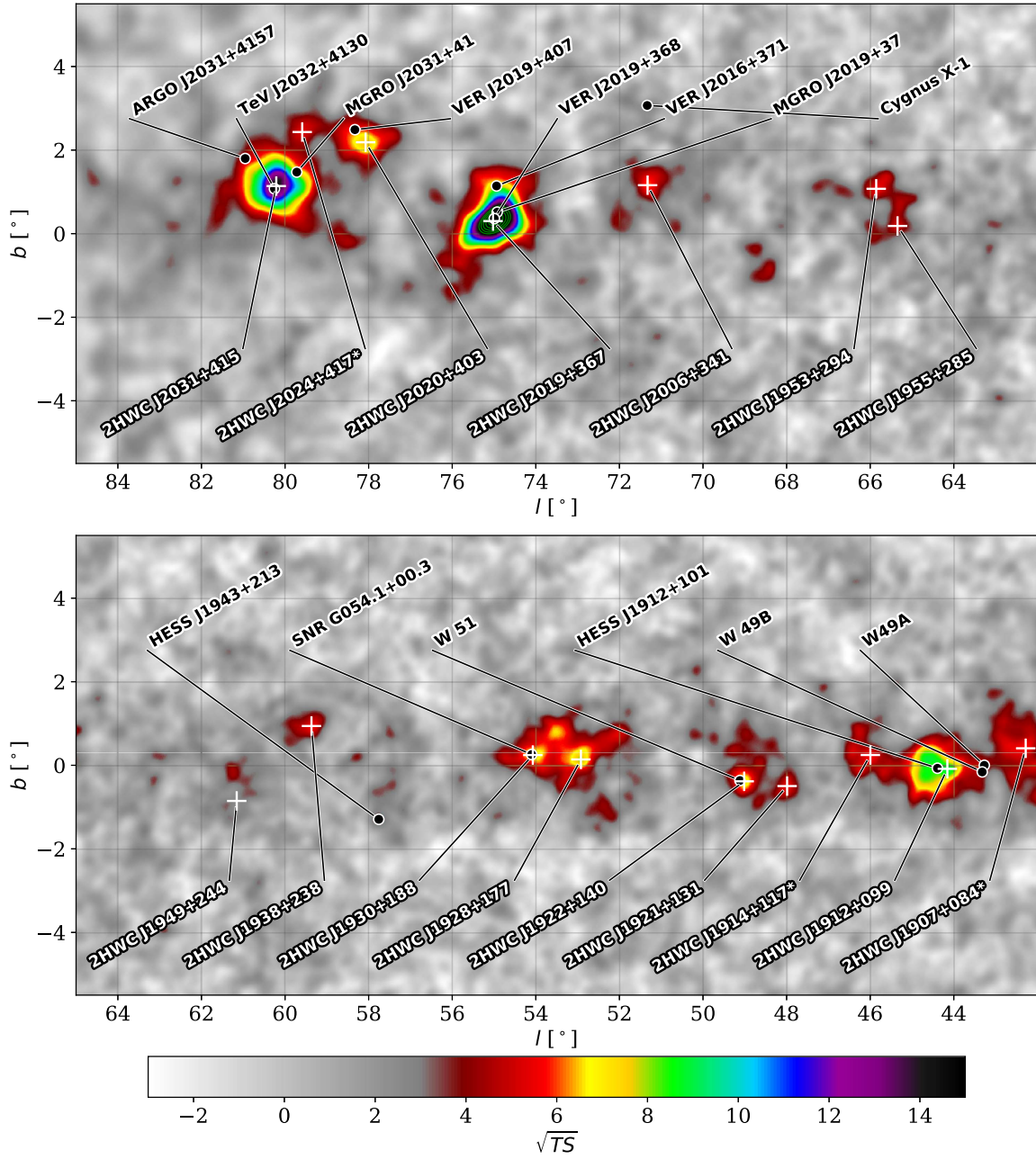
Figure 7. Parts of the inner Galactic plane region, in Galactic coordinates. The TS map corresponds to a point source hypothesis with a spectral index of −2.7. The green contour lines indicate values of $\sqrt{TS}$ of 15, 16, 17, etc. In this figure and the following, 2HWC sources are represented by white crosses and labels below; whereas the source listed in TeVCat are represented with black circles and labels above them.

emission is dominated by the pulsed emission originating from the pulsar. Although the pulsed emission has been observed up to 1.5 TeV (Ansoldi et al. 2016), most of the TeV emission is due to inverse Compton scattering in the surrounding PWN (Atoyan & Aharonian 1996).

The spectrum measured here matches previously published results. A more complete analysis of the Crab Nebula observation by HAWC will be presented in a separate publication (Abeysekara et al. 2017b).

5.2. 2HWC J0631+169 and 2HWC J0635+180—Geminga

2HWC J0631+169 and 2HWC J0635+180 are both found in the point source search, each above the TS threshold value of 25. The corresponding TS maximum in the 2° extended search

is 126. They appear to be associated with Geminga, a known GeV (Abdo et al. 2010b) gamma-ray pulsar. Prior to HAWC, Milagro was the only TeV instrument to have detected it. Milagro reported an extended source of full width at half maximum around 2°.6 (Abdo et al. 2009). The large extent of the source makes it difficult for IACTs to observe it. To date, none have reported a detection of Geminga (see, e.g., Ahnen et al. 2016).

Compared to other TeV PWNe, the powering pulsar PSR J0633+1746 is relatively old (342 kyr), nearby (250^{+120}_{-62} pc) and has a low spindown power (3.2×10^{34} erg s^{-1}). Geminga (along with PSR B0656+14) has been proposed as the dominant source of the local population of TeV electrons and positrons, and thus a possible explanation for
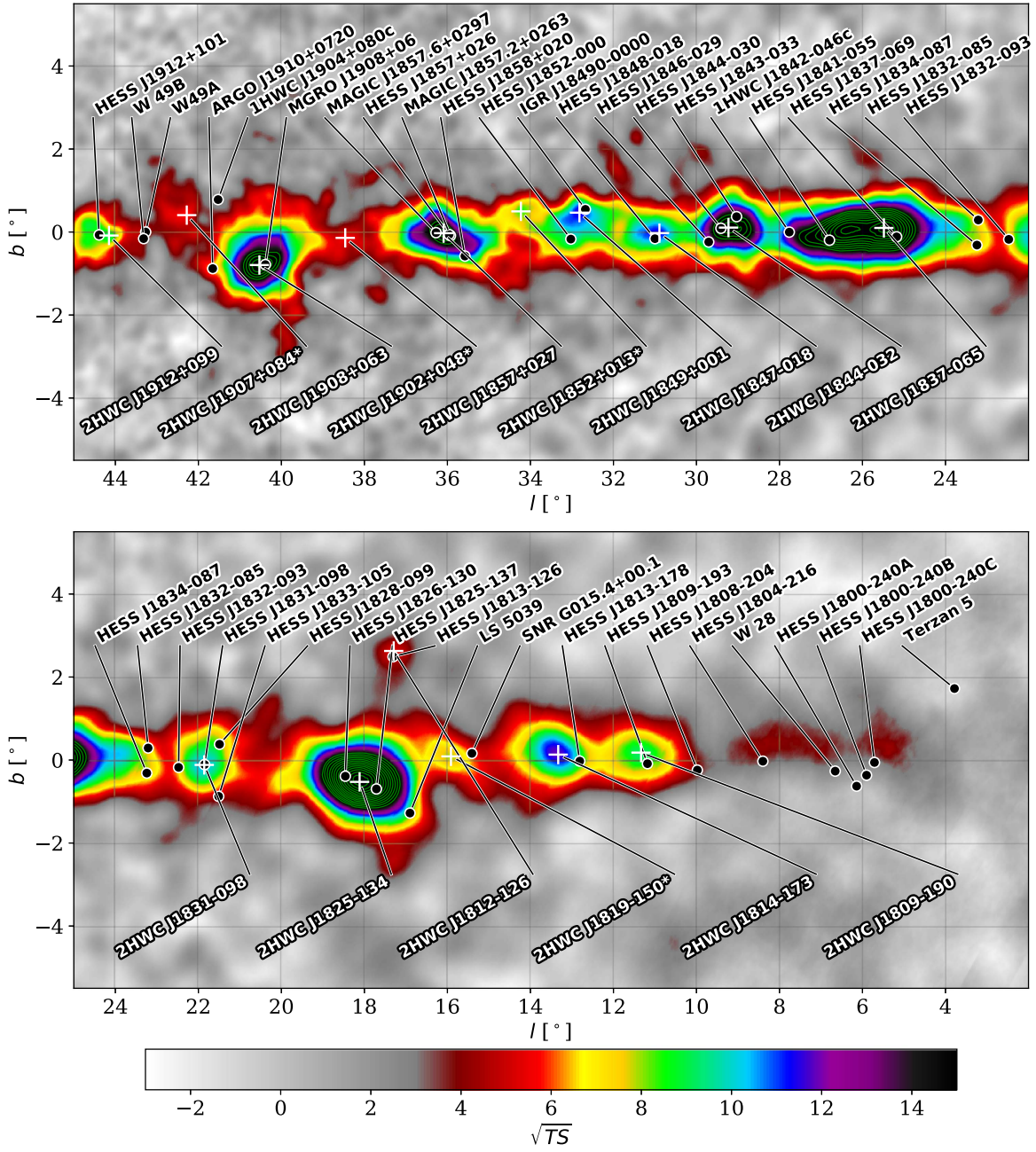
Figure 8. Same as Figure 7, but farther along the Galactic Plane.

the PAMELA positron excess (Aharonian et al. 1995; Yüksel et al. 2009).

When fitted with a uniform disk source model, the extent observed in HAWC is around 2° in radius, and the measured spectral index is relatively hard at −2.2. The measured spectrum depends on the assumed morphology. The flux measured by HAWC with a 2° radius disk model is compatible (within statistical error) with the one reported in Abdo et al. (2007), using an extended source model (2°.8 FWHM Gauss model). A detailed study of Geminga and 2HWC J0700+143 (see next section) by HAWC will be presented in a dedicated publication (HAWC Collaboration 2017, in preparation).

5.3. 2HWC J0700+143

With a TS of 29, 2HWC J0700+143 is a new TeV source discovered in the 1° extended search. The corresponding TS maximum in the 2° extended search is 51. It is associated with the B0656+14 pulsar, which has similar characteristics to the Geminga pulsar: old (111 kyr), nearby (288^{+33}_{-27} pc), and low spindown power ($3.8 \times 10^{34}\,\mathrm{erg\,s}^{-1}$) (Brisken et al. 2003). The corresponding supernova is believed to be the origin of the Monogem Ring. As for Geminga, PSR B0656+14 has been proposed as a significant contributor to the local lepton populations.

The measured extent of this source is around 2°, with a hard spectral index of about −2.

Table 2
2HWC Source List and Nearest TeVCat Sources

Name	Search	TS	R.A. (°)	Decl. (°)	l (°)	b (°)	1σ Stat. unc. (°)	Nearest TeVCat Source	
								Dist. (°)	Name
2HWC J0534+220	PS	1.1E+4	83.63	22.02	184.55	−5.78	0.06	0.01	Crab
2HWC J0631+169	PS	29.6	98.00	17.00	195.61	3.51	0.11	0.39	Geminga
2HWC J0635+180	PS	27.4	98.83	18.05	195.04	4.70	0.13	0.97	⋯
2HWC J0700+143	1°.0	29	105.12	14.32	201.10	8.44	0.80	2.98	⋯
2HWC J0819+157	0°.5	30.7	124.98	15.79	208.00	26.52	0.17	7.86	⋯
2HWC J1040+308	0°.5	26.3	160.22	30.87	197.59	61.31	0.22	8.77	⋯
2HWC J1104+381	PS	1.15E+3	166.11	38.16	179.95	65.05	0.06	0.04	Markarian 421
2HWC J1309−054	PS	25.3	197.31	−5.49	311.11	57.10	0.22	3.27	⋯
2HWC J1653+397	PS	556	253.48	39.79	63.64	38.85	0.07	0.03	Markarian 501
2HWC J1809−190	PS	85.5	272.46	−19.04	11.33	0.18	0.17	0.31	HESS J1809−193
2HWC J1812−126	PS	26.8	273.21	−12.64	17.29	2.63	0.19	0.14	HESS J1813−126
2HWC J1814−173	PS	141	273.52	−17.31	13.33	0.13	0.18	0.54	⋯
2HWC J1819−150*	PS	62.9	274.83	−15.06	15.91	0.09	0.16	0.51	⋯
2HWC J1825−134	PS	767	276.46	−13.40	18.12	−0.53	0.09	0.39	HESS J1826−130
2HWC J1829+070	PS	25.3	277.34	7.03	36.72	8.09	0.10	8.12	⋯
2HWC J1831−098	PS	107	277.87	−9.90	21.86	−0.12	0.17	0.01	HESS J1831−098
2HWC J1837−065	PS	549	279.36	−6.58	25.48	0.10	0.06	0.37	HESS J1837−069
2HWC J1844−032	PS	309	281.07	−3.25	29.23	0.11	0.10	0.18	HESS J1844−030
2HWC J1847−018	PS	132	281.95	−1.83	30.89	−0.03	0.11	0.17	HESS J1848−018
2HWC J1849+001	PS	134	282.39	0.11	32.82	0.47	0.10	0.16	IGR J18490−0000
2HWC J1852+013*	PS	71.4	283.01	1.38	34.23	0.50	0.13	1.37	⋯
2HWC J1857+027	PS	303	284.33	2.80	36.09	−0.03	0.06	0.14	HESS J1857+026
2HWC J1902+048*	PS	31.7	285.51	4.86	38.46	−0.14	0.18	2.03	⋯
2HWC J1907+084*	PS	33.1	286.79	8.50	42.28	0.41	0.27	1.15	⋯
2HWC J1908+063	PS	367	287.05	6.39	40.53	−0.80	0.06	0.14	MGRO J1908+06
2HWC J1912+099	PS	83.2	288.11	9.93	44.15	−0.08	0.10	0.24	HESS J1912+101
2HWC J1914+117*	PS	33	288.68	11.72	46.00	0.25	0.13	1.64	⋯
2HWC J1921+131	PS	30.1	290.30	13.13	47.99	−0.50	0.12	1.14	⋯
2HWC J1922+140	PS	49	290.70	14.09	49.01	−0.38	0.11	0.10	W 51
2HWC J1928+177	PS	65.7	292.15	17.78	52.92	0.14	0.07	1.18	⋯
2HWC J1930+188	PS	51.8	292.63	18.84	54.07	0.24	0.12	0.03	SNR G054.1+00.3
2HWC J1938+238	PS	30.5	294.74	23.81	59.37	0.94	0.13	2.75	⋯
2HWC J1949+244	1°.0	34.9	297.42	24.46	61.16	−0.85	0.71	3.43	⋯
2HWC J1953+294	PS	30.1	298.26	29.48	65.86	1.07	0.24	8.44	⋯
2HWC J1955+285	PS	25.4	298.83	28.59	65.35	0.18	0.14	7.73	⋯
2HWC J2006+341	PS	36.9	301.55	34.18	71.33	1.16	0.13	3.61	⋯
2HWC J2019+367	PS	390	304.94	36.80	75.02	0.30	0.09	0.07	VER J2019+368
2HWC J2020+403	PS	59.7	305.16	40.37	78.07	2.19	0.11	0.40	VER J2019+407
2HWC J2024+417*	PS	28.4	306.04	41.76	79.59	2.43	0.20	0.97	⋯
2HWC J2031+415	PS	209	307.93	41.51	80.21	1.14	0.09	0.08	TeV J2032+4130

Note. The sources with a * symbol correspond to sources that are not separated from their neighbor by a large TS gap, as defined in Section 2.

5.4. 2HWC J0819+157

This source is found in the 0°.5 radius extended search, with a TS value of 30.7. The coordinates correspond to a location outside the Galactic plane ($b = 26°.52$). The fitted index (−1.50) is much harder than that of any other source. The nearest potentially high-energy source is the AGN 2MASS J08203478+1531114, 0.3 away. However, its distance ($z = 0.14$) seems incompatible with the observed extent and hard spectrum.

5.5. 2HWC J1040+308

Similar to 2HWC J0819+157, this source is found in the 0°.5 radius extended search, with a TS value of 26.3. No associations are found in the catalogs. The coordinates correspond to a location outside the Galactic plane

($b = 61°.31$), which seems to be in tension with the source extent.

5.6. 2HWC J1104+381 and 2HWC J1653+397—Markarian 421 and Markarian 501

Markarian (Mrk) 421 and Mrk 501 are two of the closest and brightest extragalactic sources in the TeV, as well as the X-ray band. The locations of these two sources (2HWC J1104+381 for Mrk 421 and 2HWC J1653+397 for Mrk 501) are the only ones in this catalog that have confirmed extragalactic nature.

At a distance of $z \approx 0.031$ (de Vaucouleurs et al. 1991; Mao 2011), Mrk 421 is a BL Lac-type blazar that was the first extragalactic object discovered at very high energies (Punch et al. 1992). It has been extensively studied in both the spectral and time domains.

Mrk 501 is also a BL Lac-type blazar, at a distance of $z = 0.033$ (de Vaucouleurs et al. 1991; Mao 2011). This object

Table 3
The 2HWC Catalog: Source Radius, Fitted Spectrum, and Nearest TeVCat Source

Name	Tested radius (°)	Index	F_7 (10^{-15} TeV^{-1}cm^{-2}s^{-1})	Nearest TeVCat source
2HWC J0534+220	⋯	-2.58 ± 0.01	184.7 ± 2.4	Crab
2HWC J0631+169	⋯	-2.57 ± 0.15	6.7 ± 1.5	Geminga
″	2.0	-2.23 ± 0.08	48.7 ± 6.9	Geminga
2HWC J0635+180	⋯	-2.56 ± 0.16	6.5 ± 1.5	⋯
2HWC J0700+143	1.0	-2.17 ± 0.16	13.8 ± 4.2	⋯
″	2.0	-2.03 ± 0.14	23.0 ± 7.3	⋯
2HWC J0819+157	0.5	-1.50 ± 0.67	1.6 ± 3.1	⋯
2HWC J1040+308	0.5	-2.08 ± 0.25	6.6 ± 3.5	⋯
2HWC J1104+381	⋯	-3.04 ± 0.03	70.8 ± 2.9	Markarian 421
2HWC J1309−054	⋯	-2.55 ± 0.18	12.3 ± 3.5	⋯
2HWC J1653+397	⋯	-2.86 ± 0.04	56.5 ± 2.7	Markarian 501
2HWC J1809−190	⋯	-2.61 ± 0.11	80.9 ± 15.1	HESS J1809−193
2HWC J1812−126	⋯	-2.84 ± 0.16	27.4 ± 5.7	HESS J1813−126
2HWC J1814−173	⋯	-2.61 ± 0.09	88.4 ± 13.0	⋯
″	1.0	-2.55 ± 0.07	151.6 ± 18.8	⋯
2HWC J1819−150*	⋯	-2.88 ± 0.10	59.0 ± 7.9	⋯
2HWC J1825−134	⋯	-2.58 ± 0.04	138.0 ± 8.1	HESS J1826−130
″	0.9	-2.56 ± 0.03	249.2 ± 11.4	HESS J1826−130
2HWC J1829+070	⋯	-2.69 ± 0.17	8.1 ± 1.7	⋯
2HWC J1831−098	⋯	-2.80 ± 0.09	44.2 ± 4.7	HESS J1831−098
″	0.9	-2.64 ± 0.06	95.8 ± 8.0	HESS J1831−098
2HWC J1837−065	⋯	-2.90 ± 0.04	85.2 ± 4.1	HESS J1837−069
″	2.0	-2.66 ± 0.03	341.3 ± 11.3	HESS J1837−069
2HWC J1844−032	⋯	-2.64 ± 0.06	46.8 ± 3.2	HESS J1844−030
″	0.6	-2.51 ± 0.04	92.8 ± 5.2	HESS J1844−030
2HWC J1847−018	⋯	-2.95 ± 0.08	28.9 ± 2.8	HESS J1848−018
2HWC J1849+001	⋯	-2.54 ± 0.10	22.8 ± 2.9	IGR J18490−0000
″	0.8	-2.47 ± 0.05	60.8 ± 4.5	IGR J18490−0000
2HWC J1852+013*	⋯	-2.90 ± 0.10	18.2 ± 2.3	⋯
2HWC J1857+027	⋯	-2.93 ± 0.05	35.5 ± 2.5	HESS J1857+026
″	0.9	-2.61 ± 0.04	97.3 ± 4.4	HESS J1857+026
2HWC J1902+048*	⋯	-3.22 ± 0.16	8.3 ± 2.4	⋯
2HWC J1907+084*	⋯	-3.25 ± 0.18	7.3 ± 2.5	⋯
2HWC J1908+063	⋯	-2.52 ± 0.05	34.1 ± 2.2	MGRO J1908+06
″	0.8	-2.33 ± 0.03	85.1 ± 4.2	MGRO J1908+06
2HWC J1912+099	⋯	-2.93 ± 0.09	14.5 ± 1.9	HESS J1912+101
″	0.7	-2.64 ± 0.06	36.6 ± 3.0	HESS J1912+101
2HWC J1914+117*	⋯	-2.83 ± 0.15	8.5 ± 1.6	⋯
2HWC J1921+131	⋯	-2.75 ± 0.15	7.9 ± 1.5	⋯
2HWC J1922+140	⋯	-2.49 ± 0.15	8.7 ± 1.8	W 51
″	0.9	-2.51 ± 0.09	26.1 ± 3.4	W 51
2HWC J1928+177	⋯	-2.56 ± 0.14	10.0 ± 1.7	⋯
2HWC J1930+188	⋯	-2.74 ± 0.12	9.8 ± 1.5	SNR G054.1+00.3
2HWC J1938+238	⋯	-2.96 ± 0.15	7.4 ± 1.6	⋯
2HWC J1949+244	1.0	-2.38 ± 0.16	19.4 ± 4.2	⋯
2HWC J1953+294	⋯	-2.78 ± 0.15	8.3 ± 1.6	⋯
2HWC J1955+285	⋯	-2.40 ± 0.24	5.7 ± 2.1	⋯
2HWC J2006+341	⋯	-2.64 ± 0.15	9.6 ± 1.9	⋯
″	0.9	-2.40 ± 0.11	24.5 ± 4.2	⋯
2HWC J2019+367	⋯	-2.29 ± 0.06	30.2 ± 3.1	VER J2019+368
″	0.7	-2.24 ± 0.04	58.2 ± 4.6	VER J2019+368
2HWC J2020+403	⋯	-2.95 ± 0.10	18.5 ± 2.6	VER J2019+407
2HWC J2024+417*	⋯	-2.74 ± 0.17	12.4 ± 2.6	⋯
2HWC J2031+415	⋯	-2.57 ± 0.07	32.4 ± 3.2	TeV J2032+4130
″	0.7	-2.52 ± 0.05	61.6 ± 4.4	TeV J2032+4130

Note. The flux F_7 is the differential flux at 7 TeV. For some sources, an additional line indicates another spectral fit with a more extended source assumption, as indicated in Section 3.6. The uncertainties reported here are statistical only. The systematic uncertainties are 0°.1 for the position, 50% for the flux, and 0.2 for the index.

was the second blazar to be detected at very high energies (Quinn et al. 1996). On average, it is the second-brightest extragalactic object emitting in the TeV band.

The fluxes of both objects are known to exhibit strong variability on timescales down to hours or even minutes; see, for example, Gaidos et al. (1996) for Mrk 421, or Albert et al.
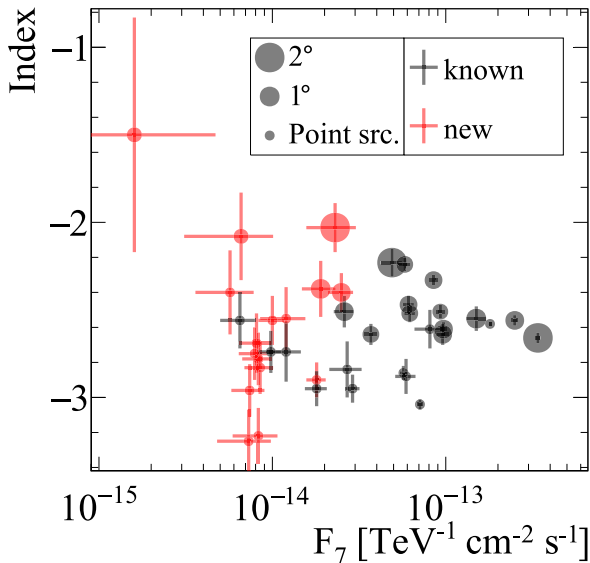
Figure 9. Distribution of the 2HWC sources in flux at 7 TeV (F_7) and power-law index. The marker size represents the source radius, which is is used to measure the spectrum and to calculate the source flux, and the color indicates whether these sources have (gray) or do not have (red) a counterpart in TeVCat.

(2007) for Mrk 501. A first look at week-long VHE flares and the time dependence of their emission observed with the partial HAWC detector is reported in Lauer & Younk (2015). Both higher and lower yearly average fluxes for Mrk 421 than the one listed in Table 3 have been reported in the past (Acciari et al. 2014). A detailed characterization of the VHE variability of Mrk 421 and Mrk 501 and a discussion of their spectral features beyond a power-law fit are presented in a separate HAWC publication (Abeysekara et al. 2017a), based on the same data discussed here, but resolved into daily time intervals.

5.7. 2HWC J1309−054

This source is found in the point search with a TS value of 25.3. No associations are found in the catalogs. The coordinates correspond to a location out of the Galactic plane ($b = 57°.1$).

5.8. 2HWC J1809−190

Source 2HWC J1809−190 is associated with HESS J1809−193 (centered ∼0°.3 away) (Aharonian et al. 2007). H.E.S.S. observed it as an extended source, modeled with an ellipse of major and minor axes 0°.53 and 0°.25, respectively. Suzaku observations confirmed hard extended X-ray emission previously detected by ASCA, and suggested a possible PWN origin (Anada et al. 2010). However, subsequent radio observations with the Expanded Very Large Array at 1.4 GHz suggested that the gamma-ray emission could instead originate from a system of molecular clouds on the edge of the SNR G11.0−0.0 shock front (Castelletti et al. 2016), and the gamma source is still considered unidentified.

5.9. 2HWC J1812−126

Source 2HWC J1812−126 is associated with the TeV source HESS J1813−126 (distance of ∼0°.1). HESS J1813−126 was recently discovered by the H.E.S.S. experiment (Deil et al. 2016), and is still unidentified. The intermediate age pulsar PSR J1813−1246, which has been also detected by *Fermi*-LAT, seems coincident with the position of the HESS source. It has a

spindown luminosity $\dot{E} = 6.2 \times 10^{36}$ erg s^{-1} and characteristic age of 43 kyr.

5.10. 2HWC J1814−173

Source 2HWC J1814−173 is located 0°.54 away from the TeV source HESS J1813−178, which was detected during the first H.E.S.S. Galactic Plane survey (Aharonian et al. 2005a; Aharonian et al. 2006b). HESS J1813−178 is a candidate PWN, powered by the highly energetic young pulsar PSR J1813−1749, located close to the center of SNR G12.82−0.02 (Gotthelf & Halpern 2009). PSR J1813−1749 has a spindown luminosity of $\dot{E} = 6.8 \times 10^{37}$ erg s^{-1}, a characteristic age of 3.3–7.5 kyr (Gotthelf & Halpern 2009), and an estimated distance of 4.8 kpc (Halpern et al. 2012). Closer to the measured HAWC location is SNR G013.5+00.2 (0°.2 away), although it has not been detected in gamma-rays by H.E.S.S. or *Fermi*-LAT .

5.11. 2HWC J1819−150*

Source 2HWC J1819−150* is located 0°.51 away from the nearest source listed in TeVCat, SNR G015.4+00.1 (HESS J1818−154). This source is reported by H.E.S.S. as a point source; given the distance to the HAWC location, this makes the identification uncertain. Closer to the measured HAWC location is SNR G015.9+00.2 (0°.1 away), although it has not been detected in gamma rays by H.E.S.S. or *Fermi*-LAT . There are also five ATNF pulsars within 0°.5 from 2HWC J1819−150*: PSR J1819−1458 (∼0°.1, $\dot{E} = 2.9 \times 10^{32}$ erg s^{-1}, $d = 3.3$ kpc, $\tau = 117$ kyr), PSR J1819−1510 (∼0°.2, $\dot{E} = 2.7 \times 10^{31}$ erg s^{-1}, $d = 4.1$ kpc, $\tau = 457$ Myr), PSR J1818−1448 (∼0°.3, $\dot{E} = 1.1 \times 10^{34}$ erg s^{-1}, $d = 5.0$ kpc, $\tau = 725$ kyr), PSR J1818−1519 (∼0°.4, $\dot{E} = 2.0 \times 10^{32}$ erg s^{-1}, $d = 5.4$ kpc, $\tau = 3.6$ Myr), and PSR J1817−1511 (∼0°.4, $\dot{E} = 5.0 \times 10^{33}$ erg s^{-1}, $d = 7.3$ kpc, $\tau = 2.5$ Myr).

5.12. 2HWC J1825−134

Source 2HWC J1825−134 was previously detected by HAWC as 1HWC J1825−1133. This source is associated with two previously reported TeV sources, HESS J1825−137 and HESS J1826−130, at about 0°.4 from both.

HESS J1826−130 was recently announced by the H.E.S.S. experiment (Deil et al. 2016), and is still unidentified. However, Angüner et al. (2017) proposed a scenario with runaway cosmic-rays colliding with dense molecular clouds to explain the very hard index. The energy spectrum of HESS J1826−130 (Angüner et al. 2017) lies about an order of magnitude below the one measured by HAWC, making the identification unlikely.

HESS J1825−137 was detected by H.E.S.S. (Aharonian et al. 2005a) and identified as a PWN (e.g., Aharonian et al. 2005b). It is connected to the energetic pulsar PSR J1826−1334 (0°.2 away from 2HWC J1825−134, $\dot{E} = 2.8 \times 10^{36}$ erg s^{-1}, $d = 3.6$ kpc, $\tau = 21$ kyr). It is generally considered the prototype of offset PWNe. HESS J1825−137 shows an energy-dependent morphology at VHE gamma rays toward the south of the pulsar PSR J1826−1334 (Aharonian et al. 2006a). The PWN identification was later confirmed by X-ray observations (Pavlov et al. 2008; Uchiyama et al. 2009), showing a clear detection of an extended PWN. The energy-dependent morphology studies of HESS J1825−137 continued in the *Fermi*-LAT era (Grondin et al. 2011; Acero et al. 2013), strengthening the key role of this source in
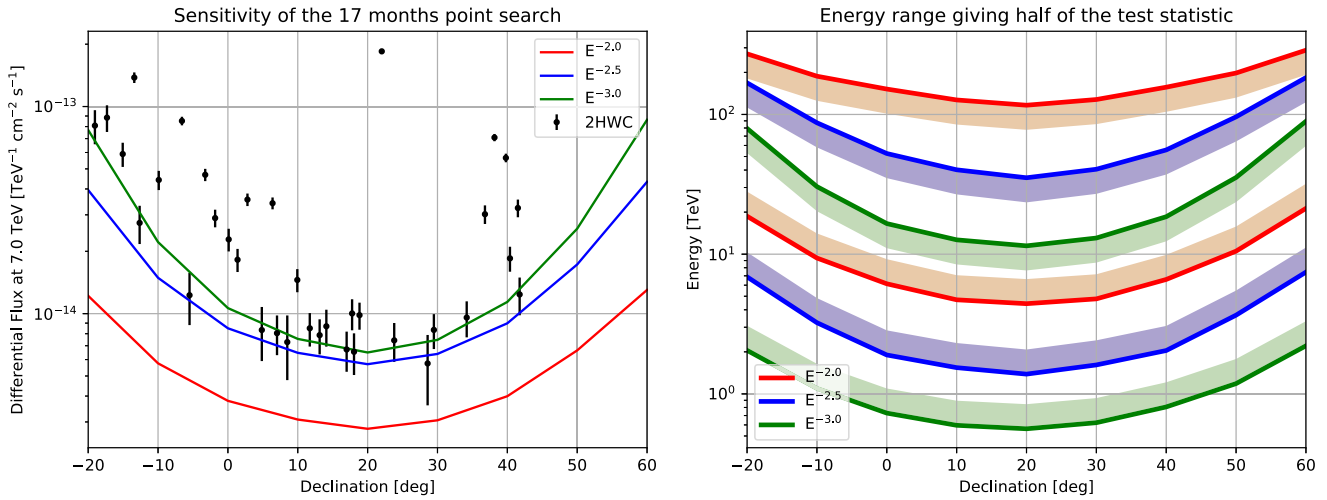
Figure 10. Left: sensitivity of the point source search for three spectral hypotheses, as a function of declination. We show the flux required to give a central expectation of 5σ, for the present analysis. The differential fluxes of the sources detected in the point source search are also shown with their statistical uncertainties. *Right*: Upper and lower ends of the energy range contributing to the central half of the test statistic of the point source search (see text).

understanding the physics of PWNe. The extension of the TeV spectrum at higher energies by HAWC is in line with this scenario, and the measured energy spectrum is compatible with the one reported by H.E.S.S. in Mitchell et al. (2017).

With more HAWC data, future analysis, including multiple source fit, will help disentangle the different components contributing to 2HWC J1825−134. We note that, in the present map, the TeV binary LS 5039 is $1°.4$ away from 2HWC J1825 −134, and is included in its TS halo in the maps presented here. Dedicated studies are being developed to separate emission from LS 5039 from 2HWC J1825−134.

5.13. 2HWC J1829+070

This source is found in the point search, with a TS value of 25.3. It is located slightly off the Galactic plane at $b = 8°.09$, and no associations are found in the catalogs.

5.14. 2HWC J1831−098

Source 2HWC J1831−098 is associated with the TeV source HESS J1831−098 (distance of $0°.01$). HESS J1831−098 was detected by the H.E.S.S. experiment in 2011 (Sheidaei 2011), and is a candidate PWN powered by the nearby 67 ms pulsar PSR J1831-0952 ($\dot{E} = 1.1 \times 10^{36}$ erg s^{-1}, $d = 3.7$ kpc, $\tau = 128$ kyr). The differential flux at 7 TeV measured by HAWC is two to five times larger than the one reported by H.E.S.S., depending on the source size used in the spectrum fit. The indices measured by HAWC are also softer than the value reported by H.E.S.S., -2.1 ± 0.1.

5.15. 2HWC J1837−065

Source 2HWC J1837−065 is the principal maximum of an elongated region containing multiple known extended sources that are not resolved in the present analysis. Source 2HWC J1837−065 is associated with the close-by TeV source HESS J1837−069 (distance of $\sim0°.4$). HESS J1837−069 can be considered a candidate PWN (Aharonian et al. 2006b; Tibolla et al. 2013). This elongated HAWC region also covers the location of the unidentified H.E.S.S. source HESS J1841−055,

which is a very complex TeV gamma-ray source with many potential counterparts, including two SNRs (Kes 73, G26.6−0.1), three high spindown pulsars: PSR J1841−0524 ($\dot{E} = 1 \times 10^{35}$ erg s^{-1}, $d = 4.1$ kpc, $\tau = 30$ kyr), PSR J1838−0549 ($\dot{E} = 1 \times 10^{35}$ erg s^{-1}, $d = 4.0$ kpc, $\tau = 112$ kyr), and PSR J1837−0604 ($\dot{E} = 2 \times 10^{33}$ erg s^{-1}, $d = 4.8$ kpc, $\tau = 34$ kyr), and an X-ray binary (AX J1841.0−0536). ARGO-YBJ also detected emission from this region, ARGO J1839-0627 (Bartoli et al. 2013a). This HAWC region will be studied further in a dedicated analysis.

5.16. 2HWC J1844−032

Source 2HWC J1844−032 was previously reported by HAWC as 1HWC J1844-031c. It is associated with two TeV gamma-ray sources: HESS J1844−030 ($\sim0°.2$ distance) and HESS J1843−033 ($\sim0°.3$ distance). The TeV-detected, well-studied, PWN Kes 75 (Djannati-Ataï et al. 2008) is slightly offset from the HAWC source ($0°.6$ away). HESS J1844−030 was recently announced by the H.E.S.S. experiment (Deil et al. 2016) and is still unidentified. The following sources are possible candidates: G29.4+0.1, AX J1844.6−0305, and PMN J1844−0306; SNR or PWN scenarios are considered reasonable. AX J1844.6−0305 was discovered by Vasisht et al. (2000) and appears in the ASCA GIS data as a bright source, and is not yet identified. PMN J1844−0306 is a complex radio/IR region, as described by Vasisht et al. (2000).

The other nearby TeV known source, HESS J1843−033 (Hoppe 2008), is a large source with several possible counterparts. A possible X-ray counterpart is AX J1843.8−0352 (G28.60.1), which is an SNR with a peculiar morphology. Chandra (Ueno et al. 2003) discovered a new source within AX J1843.8−0352, CXO J184357−035441, which exhibits a thin thermal spectrum and a jet-like tail. Other possibilities could be AX J1845.0−0258, which has been considered as an anomalous X-ray pulsar, or SNR G28.8+1.5, whose outer shells may interact with some undiscovered molecular clouds. Further multi-wavelength observations are crucial to identify the origin of the VHE emission.

5.17. 2HWC J1847−018

Source 2HWC J1847−018 was previously detected by HAWC as 1HWC J1849−017c. It is associated with the unidentified TeV gamma-ray source HESS J1848−018 (∼0°.2 distance). HESS J1848−018 was discovered by the H.E.S.S. experiment in the extended Galactic plane Survey. It is located in the direction of, but slightly offset from, the star-forming region W 43 and hence a possible association with it was suggested in Chaves et al. (2008). However, the association with the star-forming region has not been further confirmed, and this source is now considered to be a candidate PWN following recent observations by *Fermi*-LAT (Acero et al. 2013). Further multi-wavelength studies are needed to properly identify the source.

5.18. 2HWC J1849+001

Source 2HWC J1849+001 is associated with the extended TeV source HESS J1849−000 (∼0°.2 distance) (Terrier et al. 2008), which is coincident with the INTEGRAL source IGR J18490−0000. Further X-ray observations by *XMM-Newton* and *RXTE* revealed that IGR J18490−0000 is a Pulsar/PWN system, where a young and very energetic pulsar ($\dot{E} = 9.8 \times 10^{36}$ erg s^{-1}, $\tau = 43$ kyr, distance unknown) is powering the system, and a compact PWN is detected in the X-ray observations (Gotthelf et al. 2011).

5.19. 2HWC J1852+013*

Source 2HWC J1852+013* is a new TeV detection by HAWC. There is no known gamma-ray sources close to this location; the nearest is the GeV source 3FGL J1852.8+0158, located 0°.6 from the central position of 2HWC J1852+013*. Given the source location, there may be a significant contribution from Galactic diffuse emission to this source.

Multi-wavelength catalog searches reveal several pulsars, several X-ray sources and H II regions in the vicinity of 2HWC J1852+013*. Chandra observations exist of a star cluster and infrared dark cloud IRDC G34.4+0.23 and NaSt1 (WR 122), a Wolf–Rayet binary.

The following pulsars are located close by: PSR J1851+0118 (∼0°.1, $\dot{E} = 7.2 \times 10^{33}$ erg s^{-1}, $d = 5.6$ kpc, $\tau = 105$ kyr), and PSR J1850+0124 (∼0°.5, $\dot{E} = 9.5 \times 10^{33}$ erg s^{-1}, $d = 3.4$ kpc, $\tau = 5.2$ Gyr).

5.20. 2HWC J1857+027

Source 2HWC J1857+027 has been previously reported by HAWC as 1HWC J1857+023. It is associated with TeV source HESS J1857+026 (∼0°.1 away) (Aharonian et al. 2008b). The H.E.S.S. source was considered a PWN candidate (e.g., Tibolla et al. 2011), associated with PSR J1856+0245 ($\dot{E} = 4.6 \times 10^{36}$ erg s^{-1}, $d = 6.3$ kpc, $\tau = 20.6$ kyr). Recent MAGIC observations revealed that the VHE emission above 1 TeV can be spatially separated into two sources: MAGIC J1857.2+0263 and MAGIC J1857.6+0297 (Aleksić et al. 2014). They also confirmed the PWN nature of the first source, and a molecular cloud association was suggested for the second source. These two MAGIC sources are too close to be distinguishable in the HAWC analysis reported here. However, they should be resolved in future analyses, including simultaneous fits of multiple sources. The energy spectrum measured by HAWC is compatible with the ones reported by H.E.S.S. and MAGIC

(the latter being measured on a 0°.4 region encompassing both MAGIC sources), supporting the identification of 2HWC J1857+027 with these sources.

5.21. 2HWC J1902+048*

Source 2HWC J1902+048* has been tagged by the search algorithm in a region that does not have a TeV counterpart. However, it appears to be in a confused region, possibly with a large contribution of the Galactic diffuse emission, and will be better disentangled in future analysis with more data. Long Swift observations with a total of 23 ks have been performed in the region of 2HWC J1902+048*, due to gamma-ray burst GRB140610. There is no possible counterpart in the 3FGL catalog of *Fermi*-LAT. However, there are two sources from the previous catalogs within 0°.5: 1FGL J1902.3+0503c (0°.2 away) and 2FGL J1901.1+0427 (0°.5 away). Catalog searches reveal several pulsars, X-ray sources, and H II regions in the vicinity of 2HWC J1902+048*.

The three closest pulsars in the ATNF catalog are: PSR J1901+0459 (∼0°.3, $d = 12.3$ kpc), PSR J1901+0435 (∼0°.3, $\dot{E} = 1.0 \times 10^{33}$ erg s^{-1}, $d = 10.3$ kpc, $\tau = 1.3$ Myr), and PSR J1901+0510 (∼0°.3, $\dot{E} = 5.3 \times 10^{33}$ erg s^{-1}, $d = 5.9$ kpc, $\tau = 313$ kyr). These pulsars could be powering a PWN that is still undetected due to the lack of multi-wavelength observations.

5.22. 2HWC J1907+084*

Source 2HWC J1907+084* is a new TeV detection by HAWC. Given the source location and TS value (33.1), there may be a large contribution from Galactic diffuse emission to this source. Multi-wavelength catalog searches reveal several pulsars, several X-ray sources, H II regions, and a molecular cloud system coincident with or in the vicinity of 2HWC J1907+084*. The nearest *Fermi*-LAT source is 3FGL J1904.9+0818, located 0°.6 away from the central position of 2HWC J1907+084*.

The nearest pulsar from the ATNF catalog is PSR J1908+0839 (∼0°.3 away, $\dot{E} = 1.5 \times 10^{34}$ erg s^{-1}, $d = 8.3$ kpc, $\tau = 1.2$ Myr).

5.23. 2HWC J1908+063—MGRO J1908+06

Source 2HWC J1908+063 is associated with the PWN MGRO J1908+06, first discovered by the Milagro experiment (Abdo et al. 2007) and later observed by H.E.S.S. (Aharonian et al. 2009), ARGO-YBJ (Bartoli et al. 2012), VERITAS (Aliu et al. 2014a), and previously reported by HAWC as 1HWC J1907+062c. This source was considered unidentified until the advent of *Fermi*-LAT, which shed light on the nature of MGRO J1908+06 and strengthened the PWN scenario to explain its VHE gamma-ray emission (Abdo et al. 2010; Acero et al. 2013). The spectrum measured in this work (see Table 3) under the extended hypothesis is consistent with the spectra obtained by H.E.S.S., VERITAS, and MILAGRO, and lower than the ARGO-YBJ results.

5.24. 2HWC J1912+099

Source 2HWC J1912+099 is associated with TeV source HESS J1912+101 (∼0°.2 distance), which was initially proposed to be a PWN connected to the high spindown luminosity pulsar PSR J1913+1011 ($\dot{E} = 2.9 \times 10^{36}$ erg s^{-1}, $d = 4.6$ kpc, $\tau = 169$ kyr) (Aharonian et al. 2008a).

ARGO-YBJ also detected emission from this region, ARGO J1912+1026 (Bartoli et al. 2013c). The spectral index they report is consistent with the one by H.E.S.S., but the flux above 1 TeV is much higher than the value reported by H.E.S.S. In this energy band, the flux of the H.E.S.S. source corresponds to ~ 9% of the Crab Nebula flux, whereas the ARGO-YBJ source flux corresponds to ~23% of the Crab flux. This discrepancy occurred for other ARGO-YBJ sources, and has been discussed in literature (Bartoli et al. 2013b). The flux measured with HAWC using the extended source model is in agreement with the H.E.S.S. measurement. Due to the lack of multi-wavelength confirmation of the PWN scenario, and based on the detection of a shell-like morphology seen with increased observation time by H.E.S.S., Pühlhofer et al. (2015) reclassified HESS J1912+101 as an SNR candidate.

5.25. 2HWC J1914+117*

Source 2HWC J1914+117* is a new TeV detection by HAWC. Given the source location and TS value (33), there may be a large contribution of the Galactic diffuse emission to this source. Multi-wavelength catalog searches reveal several pulsars, X-ray sources, and H II regions coincident with or in the vicinity of 2HWC J1914+117*. There have been seven Swift observations, but the overall exposure is too low to identify a possible counterpart. There are no possible counterparts in the *Fermi*-LAT catalogs.

The pulsars from the ATNF pulsar catalog located in the vicinity of 2HWC J1914+117* are: PSR J1915+1144 ($0°1$, $d = 7.2$ kpc), PSR J1915+1149 ($0°1$, $d = 14$ kpc), PSR J1913+1145 ($0°2$, $\dot{E} = 6.9 \times 10^{33}$ erg s^{-1}, $d = 14$ kpc, $\tau = 967$ kyr), and PSR B1911+11 ($0°4$, $\dot{E} = 1.2 \times 10^{32}$ erg s^{-1}, $d = 3.1$ kpc, $\tau = 14.5$ Myr).

5.26. 2HWC J1921+131

Source 2HWC J1921+131 is a new TeV detection by HAWC. Given the source location and TS value (30.1), there may be a large contribution from Galactic diffuse emission to this source. Multi-wavelength catalog searches reveal several pulsars, X-ray sources, and a molecular cloud system coincident with or in the vicinity of 2HWC J1921+131. Swift observations exist of the source IGR J19203+1328. There is no possible counterpart in the *Fermi*-LAT catalogs within a radius of $1°$. PSR J1919+1314 is the only nearby pulsar from the ATNF pulsar catalog, $0°4$ away. It is an old (2.4 My) pulsar at a distance $d = 13$ kpc and not very energetic ($\dot{E} = 8 \times 10^{32}$ erg s^{-1}), making the identification unlikely.

5.27. 2HWC J1922+140—W51C

Source 2HWC J1922+140 is associated with the radio-bright SNR W51C, which is located at a distance of ~4.3 kpc (Tian & Leahy 2013) and is a middle-aged remnant (~3 × 10^4 yr) with an elliptical shape in radio encompassing a size of $0°6 \times 0°8$ (Koo et al. 1995). W51C was detected by *Fermi*-LAT in the energy range from 200 MeV to 50 GeV. Jogler & Funk (2016) reported a high-energy break in the energy spectrum of 2.7 GeV and a spectral index beyond the break at $-2.52^{+0.07}_{-0.06}$. In Aleksić et al. (2012), the MAGIC collaboration reported the detection of W51C at the 11σ level and a spectral index of $-2.58 \pm 0.07_{\rm stat} \pm 0.22_{\rm sys}$. Above 1 TeV, MAGIC observes W15C as an elongated region of half width about $0°1$ on the long axis.

Source 2HWC J1922+140 is detected by HAWC in the point source search. However, the residual map exhibits various excess around the position of the source once the point source modeled has been subtracted. This indicates that there may be additional emission farther away from W51C than previously reported. Given the source location, there may be a significant contribution from Galactic diffuse emission to this extended emission. The spectrum fit is thus performed both using a point source model and an extended source model, with radius $0°9$. The spectrum measurement reported in Table 3 under the point source hypothesis appears to be in agreement with the MAGIC and *Fermi*-LAT results, whereas the one performed with the extended hypothesis is larger by about a factor 3.

5.28. 2HWC J1928+177 and 2HWC J1930+188 Region

In this region, two sources are found in the point search: 2HWC J1928+177 and 2HWC J1930+188. Only the second source is previously detected in TeV, even though the location of the first source has been observed by IACTs. This region also exhibits signs of additional emission, which will be investigated in future analysis.

Source 2HWC J1928+177 is a new TeV source discovered in the point source search. It is associated with the pulsar PSR J1928+1746 ($0°03$ away, $\dot{E} = 1.6 \times 10^{36}$ erg s^{-1}, $d = 4.3$ kpc, $\tau = 83$ kyr), the first pulsar discovered in the Arecibo L-band Feed Array survey (Cordes et al. 2006). This pulsar and 2HWC J1928+177 are also within the 99% uncertainty region of the unidentified EGRET source 3EG J1928+1746, which shows significant variability (Hartman et al. 1999). The *Fermi*-LAT association for this EGRET source is 3FGL J1928.9+1739. However, the 3FGL source position and the 2HWC J1928+177 source position are not consistent within statistical uncertainty. Also note that *Fermi*-LAT reported two analysis flags associated with this source, indicating a significant dependency of the reported source on the choice of the background model and other possible issues with detection or characterization of the source. VERITAS has also observed the location of PSR J1928+1746 (Acciari et al. 2010). However, VERITAS only observed a 1.2σ excess at the source position, and set a flux upper limit above 1 TeV at the 99% confidence level, assuming a power law distribution with power-law index of -2.5 at 2.6×10^{-13} cm^{-2} s^{-1}. Even though the power-law index assumed by VERITAS is similar to the HAWC measured spectral index, the flux measured by HAWC is about three times larger than the VERITAS limit, which seems to indicate that the spatial extent of PSR J1928+1746 is larger than the PSF of VERITAS.

Source 2HWC J1930+188 is associated with the SNR SNR G054.1+00.3, which is a known TeV source discovered by VERITAS (Acciari et al. 2010). The VERITAS observation is consistent with a point-like source within the resolution of the instrument. SNR G054.1+00.3 hosts a young, energetic pulsar, PSR J1930+1852, at its center ($\dot{E} = 1.2 \times 10^{37}$ erg s^{-1}, $d = 7$ kpc, $\tau = 2.9$ kyr). Lu et al. (2001) report the discovery of a non-thermal X-ray jet that is consistent with a radio extension. It confirms the existence of a PWN in the SNR G054.1+00.3. The spectral indices and fluxes at 7 TeV of VERITAS and HAWC are consistent within statistical and systematic uncertainties. The HAWC measurements indicate that the TeV spectrum associated with SNR G054.1+00.3
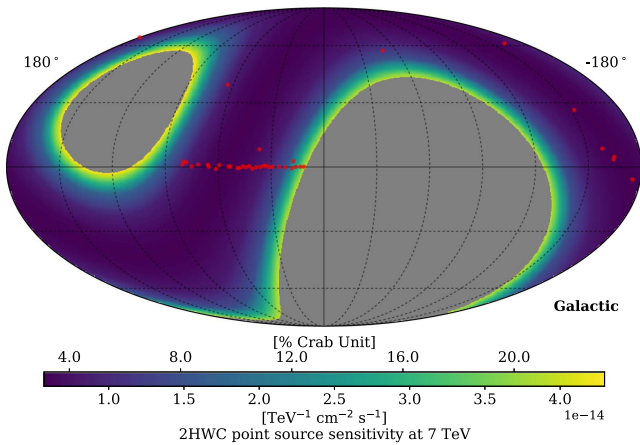
Figure 11. Sensitivity of the point source search of the 2HWC survey, represented in Galactic coordinates, and overlaid with the 2HWC source locations. The color scale corresponds to the differential flux at 7 TeV for a 50% chance of TS > 25, assuming a source of index −2.5.

extends beyond the VERITAS measured energy range (250 GeV–4 TeV).

As explained in Section 4.2, the flux has also been calculated under an extended source hypothesis. The radius has been chosen to include the region around 2HWC J1928+177 and 2HWC J1930+188. Table 3 shows that the measured flux for this whole region is significantly larger than the sum of the fluxes of 2HWC J1928+177 and 2HWC J1930+188 under the point source hypothesis, thus favoring extended emission or additional unresolved sources.

5.29. 2HWC J1938+238

Source 2HWC J1938+238 is a new TeV source discovered in the point source search, within the Galactic plane. There are several optical galaxies, radio galaxies, and an ATNF pulsar within 0°.5 around the source location. However, none of these sources are known X-ray or gamma-ray sources. The pulsar, PSR J1940+2337, is located 0°.4 away from 2HWC J1938 +238. It is a middle-aged pulsar (113 kyr) with a spindown power $\dot{E} = 1.9 \times 10^{34}$ erg s^{-1} and a distance $d = 8.5$ kpc.

5.30. 2HWC J1949+244

Source 2HWC J1949+244 is a new TeV source discovered within the Galactic plane. The source is discovered in the 1° extended search; given the low latitude of the source, this suggests that there can be an important contribution of the Galactic diffuse emission to this source, up to about 40% of the measured flux. It is located 0°.1 away from the unidentified Fermi-LAT source 3FGL J1949.3+2433. The extent of 3FGL J1949.3+2433 is less than 0°.1, which is much smaller than the size of the search in which 2HWC J1949+244 was found. The Fermi-LAT measured spectral index of this source is −2.8 ± 0.2, which is slightly softer than the one measured by HAWC.

The millisecond pulsar PSR J1950+2414 is also located near 2HWC J1949+244 (0°.3, $\dot{E} = 9.4 \times 10^{33}$ erg s^{-1}, $d = 7.3$ kpc, $\tau = 3.6$ Gyr). However, this source has not been detected in X-ray or GeV (Knispel et al. 2015).

5.31. 2HWC J1953+294 and 2HWC J1955+285 Region

In this region, two sources are found nearby in the point source search: 2HWC J1953+294 and 2HWC J1955+285, neither of which has previous TeV detection.

After the HAWC discovery of 2HWC J1953+294, VERITAS observed this source for 37 hr and confirmed the existence of the TeV source. The VERITAS observations of this source will be continued during the 2016–2017 season (Holder 2017). Source 2HWC J1953+294 is located at 0°.2 from the PWN DA 495, which is associated with the SNR G65.7+1.2. It is likely that the 3FGL J1951.6+2926 is associated with the central pulsar of this system (Karpova et al. 2015). A joint analysis of this region with Fermi-LAT, VERITAS, and HAWC data is ongoing.

The second new source, 2HWC J1955+285, may be associated with the shell-type SNR SNR G065.1+00.6, located 0°.5 away. The first gamma-ray source in the region of SNR G065.1+00.6 was reported by the COS-B satellite as 2CG 065 +00 (Swanenburg et al. 1981), then confirmed by the EGRET detection 3EG J1958+2909 (Hartman et al. 1999). Source 2HWC J1955+285 is near the energetic Fermi-LAT pulsar PSR J1954+2836 (0°.2 away, $\dot{E} = 1.0 \times 10^{36}$ erg s^{-1}, $\tau = 69$ kyr). Fermi-LAT also reported a non-observation of the SNR in Acero et al. (2016). Milagro reported a 4.3σ excess at this location (Abdo et al. 2009). MAGIC reported a non-detection, and set a flux limit at 2%–3% of the Crab Nebula flux at 1 TeV (Aleksic et al. 2010).

5.32. Cygnus Region

Within Galactic longitude 70° and 85° along the Galactic plane, there are five 2HWC sources. One is potentially part of the very extended emission in the Cygnus Cocoon field, and the rest are mostly associated with known TeV gamma-ray sources.

Source 2HWC J2006+341 is observed with a TS value of 36.9 and unassociated with any known TeV detections. Milagro has reported a 3.3σ excess at this location. The nearest gamma-ray source is 0°.7 away, an unidentified Fermi-LAT source 3FGL J2004.4+3338. This source was also reported in the 1FHL catalog but not the 2FHL catalog. Within a 1° radius, there are no nearby SNRs from the Manitoba catalog. The nearest pulsar from the ATNF pulsar catalog is PSR J2004+3429, 0°.4 away. Its characteristics are $d = 11$ kpc, $\dot{E} = 5.8 \times 10^{35}$ erg s^{-1}, and a characteristic age of 18 kyr.

Source 2HWC J2019+367 is associated with MGRO J2019 +37, which has a reported extent of 0°.7 from a 2D Gaussian fit (Abdo et al. 2012). The extended Milagro source is resolved into two by VERITAS (Aliu et al. 2014c), VER J2016+371 and VER J2019+368, with brighter emission coming from the latter. The nature of VER J2016+371 is unclear and could be associated with either the SNR CTB 87 or a blazar; both have been detected by Fermi-LAT. VER J2019+368 is extended and encompasses two pulsars: PSR J2021+3651 (3FGL J2021.1+3651) and PSR J2017+3625 (3FGL J2017.9 +3627), as well as a star-forming region Sh 2-104, all of which could contribute to the extended TeV emission (Gotthelf et al. 2016). The spectrum of VER J2019+368 is derived from a circular region of 0°.5 radius. It is very hard, with a photon index of −1.75 ± 0.3 up to 30 TeV. Comparing the integrated flux between 1 and 30 TeV, the 2HWC measurement from a point source assumption is still higher than that of the
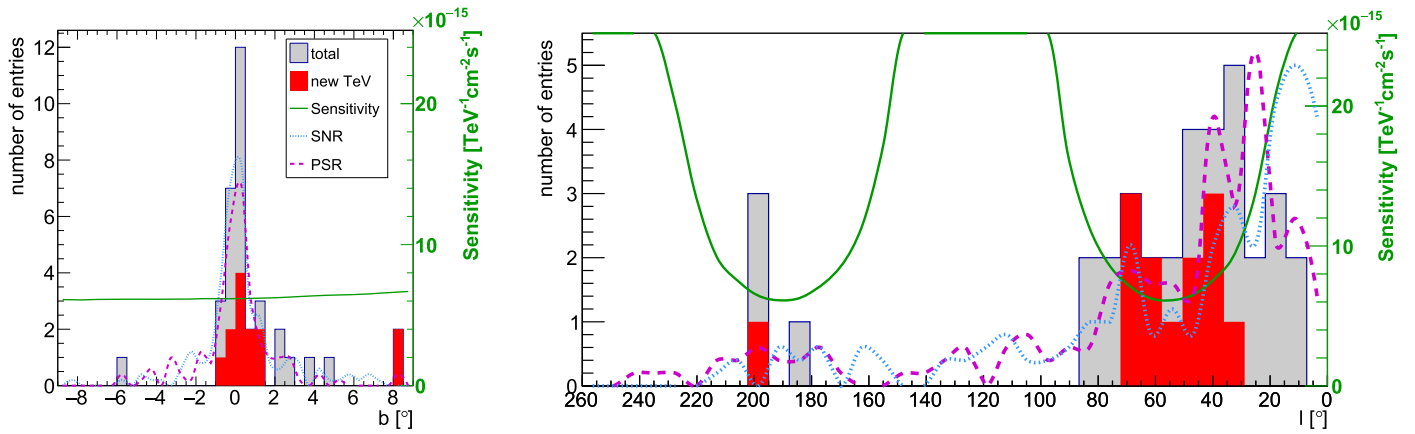
Figure 12. Left: Galactic latitude distribution of 2HWC catalog sources in bins of $\Delta b = 0°.5$. Right: Galactic longitude distribution in bins of $\Delta l = 7°.2$. The subset of sources without a TeVCat association are shown in red. The right-hand axis on the plot indicate the differential point-source flux sensitivity of the survey at 7 TeV. In the case of the b-distribution, the sensitivity at $l = 60°$ is indicated by the green line and for the l-distribution the sensitivity is shown for $b = 0°$. Both distributions are compared to distributions of known pulsars (Manchester et al. 2005) and supernova remnants (Green 2014) in the field of view of HAWC. Both pulsars and supernova remnants distributions are binned in the same way as the 2HWC sources, and re-scaled for ease of comparison. In addition, only pulsars with a spindown luminosity of $\dot{E} > 10^{34}$ erg s^{-1} are indicated.

VERITAS extended assumption. The PSF of this HAWC data set below 1 TeV is more extended than the 0°.5 radius used by VERITAS, and the source could be more extended than previously thought. The integrated flux from the extended source fit of the HAWC source is more consistent with the Milagro measurement.

Source 2HWC J2020+403 is likely associated with VER J2019+407 (Aliu et al. 2013). TeV emission from this source is unidentified, and potentially associated with the SNR G78.2+2.1 (e.g., Fraija & Araya 2016) or the gamma-ray pulsar PSR J2021 +4026 ($\dot{E} = 1.2 \times 10^{35}$ erg s^{-1}, $d = 2.1$ kpc, $\tau = 77$ kyr). The SNR G78.2+2.1 (Gamma Cygni) is detected as extended by *Fermi*-LAT, and reported in both the 3FGL and the 2FHL catalogs. The flux observed by HAWC is higher than the one reported from VER J2019+407. HAWC may be measuring multiple emission components.

Diffuse emission in this region with a 2D Gaussian width of $(2.0 \pm 0.2)°$ has been reported by the Fermi collaboration (Ackermann et al. 2011). The GeV diffuse emission is named the Cygnus Cocoon, and likely originates from a superbubble of freshly accelerated cosmic rays that are confined up to 150 TeV. ARGO J2031+4157 is reported as the counterpart of the Cygnus Cocoon (Bartoli et al. 2014). The 2D Gaussian width of this source is measured to be $(1.8 \pm 0.5)°$, after subtraction of nearby known TeV sources. This is in agreement with the extended emission reported by Milagro, which has a 2D Gaussian width of 1°.8 and a spectrum compatible with an extrapolation of the Fermi Cocoon spectrum (Abdo et al. 2012).

Source 2HWC J2031+415 is associated with TeV J2031 +4130, a PWN first reported as unidentified in TeV by HEGRA (Aharonian et al. 2002). Various IACTs have reported point-like or up to 0°.2 extended emissions from the pulsar position, with consistent spectra (Lang et al. 2004; Albert et al. 2008; Aliu et al. 2014b). Milagro and ARGO have reported extended emission compatible with the Cygnus Cocoon, as mentioned above. The HAWC flux is more consistent with the flux measured by Milagro and ARGO than the IACTs, in agreement with possible additional emission components besides the PWN within the region.

Source 2HWC J2024+417* is detected with TS = 28.4 and could be part of the extended morphology of 2HWC J2031 +415. It is 0°.35 from 3FGL J2023.5+4126, which is associated with the Cygnus Cocoon field. In addition to the diffuse emission, the 3FGL catalog also lists multiple sources associated with the Cygnus Cocoon field.

6. Source Population

A total of 39 sources are reported in the 2HWC catalog: twenty of them are associated with TeVCat sources (i.e., less than 0°.5 away), and the remaining nineteen are unassociated. Out of the twenty associated sources, 10 are reported in TeVCat as identified as PWN or SNR, two as blazars, and the remaining eight are unidentified.

The location of the 2HWC sources are represented on Figure 11, overlaid with the sensitivity of the survey, which is very uniform over a large fraction of the sky. The majority of the sources in the catalog lie near the Galactic plane. Figure 12 illustrates the distributions of the sources in Galactic latitude b and longitude l, as well as the sensitivity, for sources within 10° from the Galactic plane. It can be seen that our sensitivity is highly uniform in a wide band around the Galactic plane ($-10° < b < 10°$). The point source flux sensitivity, as presented in Figure 11, allows us to survey a wide range of Galactic latitudes. Indeed, two new sources are found at rather large Galactic latitudes: 2HWC J0700+143 at $b = 8°.44$ and 2HWC J1829+070 at $b = 8°.09$). However, the distribution of the newly detected sources peaks within $|b| < 1°$. In Figure 12, the total and new 2HWC source distributions are compared to the known distributions of SNRs from Green (2014) and pulsars with a spindown luminosity $\dot{E} > 10^{34}$ erg s^{-1} from Manchester et al. (2005). When taking into account the sensitivity of this catalog in l, the distribution of the new sources is broadly consistent with that of known SNRs and PSRs.

As noted earlier, in the Inner Galactic plane, Galactic diffuse emission may have a significant impact on the flux measurement of some sources near the TS threshold. Current knowledge of this emission in the TeV regime is limited, and HAWC is uniquely suited to measure this Galactic diffuse emission in the future.

Out of the Galactic plane, 2HWC J1104+381 (Mrk421) and 2HWC J1653+397 (Mrk 501) are the only sources with known extragalactic association. We also detect four sources, which have no association, but are also very close to the TS threshold, indicating that they may be statistical fluctuations. Random fluctuations are expected to appear mostly out of the Galactic plane because the latter only represents a small fraction of the sky. However, the expected number of false positive in the catalog search is 0.5, so we regard these sources as interesting and certainly worthy of further scrutiny. Overall, the extragalactic sources represent a smaller fraction of the total number of sources than typically observed by other gamma-ray instruments (e.g., >75% of extragalactic sources in *Fermi*-LAT 2FHL, and about 50% for IACTs in TeVCat). This is due to the sensitivity of HAWC peaking at higher energy than satellites and IACTs, energy where VHE gamma rays are attenuated by interaction with the EBL.

7. Conclusions

The 2HWC catalog is the result of the first search performed with 507 days of data from the fully deployed HAWC Observatory. It is the most sensitive unbiased TeV survey of large regions of the northern sky performed to date. The peak sensitivity of this survey lies around 10 TeV, depending on the source spectrum. This allowed the detection of a total of 39 sources, 19 of which are new sources, more than $0°.5$ away from sources reported in TeVCat. The source characteristics (location, spectrum, and for some, a tentative indication of the extent) were presented, and associations were discussed. Some sources are in complex regions with nearby sources, and refined analysis, as well as more statistics, will help the source identification. Four sources are found in the extended search only.

HAWC is continuously taking data, and the analysis and detector modeling are being refined. A high-energy extension of the HAWC detector, the outrigger array, is also under deployment. Future analyses will include more data, and explore the modeling of multiple sources and detailed morphologies, making use of multi-instrument and multi-wavelength information. Joint efforts with other current instruments are ongoing, including both allocation of observation time and joint analysis. The next generation of observatories, including LHAASO (Sciascio 2016) and CTA (Acharya et al. 2013), should allow the TeV sky to be surveyed with greater sensitivity.

References

Abdo, A., Allen, B. T., Aune, T., et al. 2009, ApJL, 700, L127
Abdo, A. A., Abeysekara, U., Allen, B. T., et al. 2012, ApJ, 753, 159
Abdo, A. A., Ackermann, M., Ajello, M., et al. 2010, ApJ, 711, 64
Abdo, A. A., Ackermann, M., Ajello, M., et al. 2010a, ApJS, 188, 405
Abdo, A. A., Ackermann, M., Ajello, M., et al. 2010b, ApJ, 720, 272
Abdo, A. A., Ajello, M., Allafort, A., et al. 2013, ApJS, 208, 17
Abdo, A. A., Allen, B., Aune, T., et al. 2008, ApJ, 688, 1078
Abdo, A. A., Allen, B., Berley, D., et al. 2007, Astroparticle Physics Letters, 664, L91
Abeysekara, A., Albert, A., Alfaro, R., et al. 2017a, ApJ, 843, 39
Abeysekara, A., Albert, A., Alfaro, R., et al. 2017b, ApJ, 841, 100
Abeysekara, A., Alfaro, R., Alvarez, C., et al. 2016, ApJ, 817, 3
Abramowski, A., Aharonian, F., Ait Benkhali, F., et al. 2014, PhRvD, 90, 122007
Acciari, V. A., Aliu, E., Arlen, T., et al. 2010, ApJL, 719, L69
Acciari, V. A., Aliu, E., Arlen, T., et al. 2011, ApJ, 738, 25
Acciari, V. A., Arlen, T., Aune, T., et al. 2014, APh, 54, 1
Acero, F., Ackermann, M., Ajello, M., et al. 2013, ApJ, 773, 77
Acero, F., Ackermann, M., Ajello, M., et al. 2015, ApJS, 218, 23
Acero, F., Ackermann, M., Ajello, M., et al. 2016, ApJS, 224, 8
Acharya, B., Actis, M., Aghajani, T., et al. 2013, APh, 43, 3
Ackermann, M., Ajello, M., Allafort, A., et al. 2011, Sci, 334, 1103
Ackermann, M., Ajello, M., Allafort, A., et al. 2013, ApJS, 209, 34
Ackermann, M., Ajello, M., Atwood, W. B., et al. 2016, ApJS, 222, 5
Aharonian, F., Akhperjanian, A., Beilicke, M., et al. 2002, A&A, 393, L37
Aharonian, F., Akhperjanian, A. G., Anton, G., et al. 2009, A&A, 499, 723
Aharonian, F., Akhperjanian, A. G., Aye, K.-M., et al. 2004, APh, 22, 109
Aharonian, F., Akhperjanian, A. G., Aye, K.-M., et al. 2005a, Sci, 307, 1938
Aharonian, F., Akhperjanian, A. G., Barres de Almeida, U., et al. 2008a, A&A, 484, 435
Aharonian, F., Akhperjanian, A. G., Barres de Almeida, U., et al. 2008b, A&A, 477, 353
Aharonian, F., Akhperjanian, A. G., Bazer-Bachi, A. R., et al. 2006a, A&A, 460, 365
Aharonian, F., Akhperjanian, A. G., Bazer-Bachi, A. R., et al. 2006b, ApJ, 636, 777
Aharonian, F., Akhperjanian, A. G., Bazer-Bachi, A. R., et al. 2007, A&A, 472, 489
Aharonian, F. A., Akhperjanian, A. G., Barrio, J. A., et al. 2001, A&A, 366, 62
Aharonian, F. A., Akhperjanian, A. G., Bazer-Bachi, A. R., et al. 2005b, A&A, 442, L25
Aharonian, F. A., Atoyan, A. M., & Voelk, H. J. 1995, A&A, 294, L41
Ahnen, M. L., Ansoldi, S., Antonelli, L. A., et al. 2016, A&A, 591, A138
Albert, J., Aliu, E., Anderhub, H., et al. 2006, ApJL, 638, L101
Albert, J., Aliu, E., Anderhub, H., et al. 2008, ApJL, 675, L25
Albert, J., Aliu, E., Anderhub, H., et al. 2007, ApJ, 669, 862
Aleksić, J., Alvarez, E. A., Antonelli, L. A., et al. 2012, A&A, 541, A13
Aleksić, J., Ansoldi, S., Antonelli, L. A., et al. 2014, A&A, 571, A96
Aleksić, J., Ansoldi, S., Antonelli, L. A., et al. 2016, APh, 72, 61
Aleksic, J., Antonelli, L. A., Antoranz, P., et al. 2010, ApJ, 725, 1629
Aliu, E., Archambault, S., Arlen, T., et al. 2013, ApJ, 770, 93
Aliu, E., Archambault, S., Aune, T., et al. 2014a, ApJ, 787, 166
Aliu, E., Aune, T., Behera, B., et al. 2014b, ApJ, 783, 16
Aliu, E., Aune, T., Behera, B., et al. 2014c, ApJ, 788, 78
Anada, T., Bamba, A., Ebisawa, K., & Dotani, T. 2010, PASJ, 62, 179
Anderhub, H., Backes, M., Biland, A., et al. 2011, NIMPA, 639, 58
Angüner, E. O., Aharonian, F., Bordas, P., et al. 2017, in AIP Conf. Proc. 1792, 6th International Symposium on High Energy Gammy-Ray Astronomy (Melville, NY: AIP), 040024
Ansoldi, S., Antonelli, L. A., Antoranz, P., et al. 2016, A&A, 585, A133
Atkins, R., Benbow, W., Berley, D., et al. 2003, ApJ, 595, 803
Atkins, R., Benbow, W., Berley, D., et al. 2004, ApJ, 608, 680
Atoyan, A. M., & Aharonian, F. A. 1996, MNRAS, 278, 525
Bacci, C., Bao, K., Barone, F., et al. 2002, APh, 17, 151
Bartoli, B., Bernardini, P., Bi, X. J., et al. 2012, ApJ, 760, 110
Bartoli, B., Bernardini, P., Bi, X. J., et al. 2013a, arXiv:1303.1258
Bartoli, B., Bernardini, P., Bi, X. J., et al. 2013b, ApJ, 767, 99
Bartoli, B., Bernardini, P., Bi, X. J., et al. 2013c, ApJ, 779, 27
Bartoli, B., Bernardini, P., Bi, X. J., et al. 2014, ApJ, 790, 152
Brisken, W. F., Thorsett, S. E., Golden, A., & Gross, W. M. 2003, ApJL, 593, L89

Carrigan, S., Brun, F., Chaves, R. C. G., et al. 2013, arXiv:1307.4690
Castelletti, G., Giacani, E., & Petriella, A. 2016, A&A, 587, A71
Chaves, R. C. G., Renaud, M., Lemoine-Goumard, M., & Goret, P. 2008, in AIP Conf. Ser. 1085, 4th International Meeting on High Energy Gamma-Ray Astronomy (Melville, NY: AIP), 372
Cordes, J. M., Freire, P. C. C., Lorimer, D. R., et al. 2006, ApJ, 637, 446
de Vaucouleurs, G., de Vaucouleurs, A., Corwin, H. G., Jr., et al. 1991, Third Reference Catalogue of Bright Galaxies (New York: Springer)
Deil, C., Brun, F., Carrigan, S., et al. 2016, ICRC (The Hague), 34, 773
Djannati-Ataï, A., deJager, O. C., Terrier, R., Gallant, Y. A., & Hoppe, S. 2008, ICRC, 2, 823
Fraija, N., & Araya, M. 2016, ApJ, 826, 31
Gaidos, J. A., Akerlof, C. W., Biller, S., et al. 1996, Natur, 383, 319
Górski, K. M., Hivon, E., Banday, A. J., et al. 2005, ApJ, 622, 759
Gotthelf, E. V., & Halpern, J. P. 2009, ApJL, 700, L158
Gotthelf, E. V., Halpern, J. P., Terrier, R., & Mattana, F. 2011, ApJL, 729, L16
Gotthelf, E. V., Mori, K., Aliu, E., et al. 2016, ApJ, 826, 25
Green, D. A. 2014, BASI, 42, 47
Grondin, M.-H., Funk, S., Lemoine-Goumard, M., et al. 2011, ApJ, 738, 42
Halpern, J. P., Gotthelf, E. V., & Camilo, F. 2012, ApJL, 753, L14
Hartman, R. C., Bertsch, D. L., Bloom, S. D., et al. 1999, ApJS, 123, 79
Holder, J. 2017, in AIP Conf. Proc. 1792, 6th International Meeting on High Energy Gamma-Ray Astronomy (Melville, NY: AIP), 020013
Holder, J., Atkins, R. W., Badran, H. M., et al. 2006, APh, 25, 391
Hoppe, S. 2008, ICRC (Mexico City), 2, 579
Jogler, T., & Funk, S. 2016, ApJ, 816, 100
Karpova, A., Zyuzin, D., Danilenko, A., & Shibanov, Y. 2015, MNRAS, 453, 2241
Knispel, B., Lyne, A. G., Stappers, B. W., et al. 2015, ApJ, 806, 140
Koo, B.-C., Kim, K.-T., & Seward, F. D. 1995, ApJ, 447, 211
Lang, M. J., Carter-Lewis, D. A., Fegan, D. J., et al. 2004, A&A, 423, 415
Lauer, R. J., & Younk, P. W. 2015, arXiv:1508.04479
Lu, F. J., Aschenbach, B., Song, L. M., & Durouchoux, P. 2001, ApSSS, 276, 141

Manchester, R. N., Hobbs, G. B., Teoh, A., & Hobbs, M. 2005, AJ, 129, 1993
Mao, L. S. 2011, NewA, 16, 503
Mitchell, A. M. W., Mariaud, C., Eger, P., et al. 2017, in AIP Conf. Proc. 1792, 6th International Meeting on High Energy Gamma-Ray Astronomy (Melville, NY: AIP), 040035
Nolan, P. L., Abdo, A. A., Ackermann, M., et al. 2012, ApJS, 199, 31
Pavlov, G. G., Kargaltsev, O., & Brisken, W. F. 2008, ApJ, 675, 683
Popkow, A., et al. 2015, arXiv:1508.06684
Pühlhofer, G., Brun, F., Capasso, M., et al. 2015, arXiv:1509.03872
Punch, M., Akerlof, C. W., Cawley, M. F., et al. 1992, Natur, 358, 477
Quinn, J., Akerlof, C. W., Biller, S., et al. 1996, Astroparticle Physics Letters, 456, L83
Sciascio, G. D. 2016, Nuclear and Particle Physics Proceedings, 279, 166
Sheidaei, F. 2011, ICRC, 7, 244
Strong, A. W., Moskalenko, I. V., & Ptuskin, V. S. 2007, ARNPS, 57, 285
Swanenburg, B. N., Bennett, K., Bignami, G. F., et al. 1981, ApJL, 243, L69
Terrier, R., Mattana, F., Djannati-Atai, A., et al. 2008, in AIP Conf. Ser. 1085, 4th International Meeting on High Energy Gamma-Ray Astronomy (Melville, NY: AIP), 312
Tian, W. W., & Leahy, D. A. 2013, ApJL, 769, L17
Tibolla, O., Mannheim, K., Kaufmann, S., & Elsässer, D. 2011, ICRC (Beijing), 6, 202
Tibolla, O., Vorster, M., Kaufmann, S., Ferreira, S., & Mannheim, K. 2013, arXiv:1306.6833
Uchiyama, H., Matsumoto, H., Tsuru, T. G., Koyama, K., & Bamba, A. 2009, PASJ, 61, S189
Ueno, M., Bamba, A., Koyama, K., & Ebisawa, K. 2003, ApJ, 588, 338
Vasisht, G., Gotthelf, E. V., Torii, K., & Gaensler, B. M. 2000, ApJL, 542, L49
Wakely, S. P., & Horan, D. 2008, ICRC (Mexico City), 3, 1341
Weekes, T. C., Cawley, M. F., Fegan, D. J., et al. 1989, ApJ, 342, 379
Younk, P. W., Lauer, R. J., Vianello, G., et al. 2016, ICRC (The Hague), 34, 948
Yüksel, H., Kistler, M. D., & Stanev, T. 2009, PhRvL, 103, 051101